P. A. Wales[1,2,†], C. A. Keller[1,3,†], K. E. Knowland[1,3,†], S. Pawson[1], S. Choi[4,5], F. Hendrick[6], M. Van Roozendael[6], R. J. Salawitch[7,8], R. Suleiman[9], W. F. Swanson[10]

[1] Global Modeling and Assimilation Office, NASA Goddard Space Flight Center, Greenbelt MD

[2] NASA Postdoctoral Program, Universities Space Research Association, Columbia MD

[3] Goddard Earth Science Technology & Research, Universities Space Research, Association, Columbia, MD

[4]Atmospheric Chemistry and Dynamics Laboratory, NASA Goddard Space Flight Center, Greenbelt, MD

[5] Science Systems and Applications, Inc., Lanham, MD

[6] Royal Belgian Institute for Space Aeronomy (BIRA-IASB), Brussels, Belgium

[7] Department of Atmospheric and Oceanic Sciences, University of Maryland, College Park, MD

[8] Earth System Science Interdisciplinary Center, University of Maryland, College Park, MD

[9] Harvard-Smithsonian Center for Astrophysics, Cambridge, MA

[10] Department of Chemistry and Biochemistry and Geophysical Institute, University of Alaska Fairbanks, Fairbanks, AK

† Now: Goddard Earth Sciences Technology & Research II, Morgan State University, Baltimore, MD

Corresponding author: Pamela Wales (pamela.a.wales@nasa.gov)

Key Points:

- We present emission estimates of Arctic bromine for 2008 – 2012 that are derived from satellite-based hotspots of bromine monoxide (BrO)
- BrO hotspots are isolated from satellite signals using the GEOS-Chem module and a statistical threshold to account for model uncertainties
- Emission fields and the resulting impact on surface ozone are sensitive to how much of the BrO signal is attributed to polar emissions

Abstract

During polar spring, periods of elevated tropospheric bromine known as "bromine explosion events" are associated with near complete removal of surface ozone. The satellite-based Ozone Monitoring Instrument (OMI) provides total column measurements of bromine monoxide (BrO) with daily global coverage. In this study, we estimate springtime bromine emissions over the Arctic using OMI retrievals of BrO in combination with the GEOS-Chem (version

12.0.1) chemical mechanism, run online within the GEOS Earth System Model. Tropospheric hotspots of BrO are identified over the Arctic where the difference between OMI and modeled columns of BrO exceeds the bias observed over regions not impacted by bromine explosion emissions. The resulting hotspot columns are a lower-limit estimate for the portion of the OMI BrO signal attributable to bromine explosion events and are well correlated with BrO measured in the lower troposphere by buoy-based instruments. Daily flux of molecular bromine is calculated from hotspot columns of BrO based on the modeled atmospheric lifetime of inorganic bromine in the lower troposphere and partitioning of bromine species into BrO at OMI overpass time. Following the application of Arctic emissions in GEOS-Chem, OMI-based tropospheric hotspots of BrO are successfully modeled for 2008 – 2012 and periods of isolated, large ($> 50\%$) decreases in surface ozone are captured during April and May. While this technique does not fully capture the low ozone observed at coastal stations, if a lower threshold is used to identify tropospheric hotspots of BrO, the representation of surface ozone in late spring is improved.

Plain Language Summary

During polar spring, high mixing ratios of brominated species drive near complete removal of surface ozone (O_3), impacting the tropospheric oxidative capacity and the biological uptake of mercury. Global models currently have multiple mechanisms for representing the underlying processes that produce bromine in polar regions. We present a novel method for estimating polar bromine emissions from measurements of bromine monoxide (BrO) collected over the Arctic by a satellite instrument. An atmospheric model is used to estimate how much of the satellite-detected BrO signal is due to background processes and isolate the portion of the signal likely associated with polar emissions. We account for uncertainties in modeled background BrO using a statistical threshold and focus our initial efforts on developing a conservative, lower-limit estimate of Arctic emissions. Our implementation of these emissions in model simulations successfully reproduces the satellite-based hotspots of BrO detected over the Arctic and captures low O_3 mixing ratios measured in late spring, while typically missing low O_3 events observed in March. The amount of bromine attributed to polar processes and the resulting impact on O_3 are highly sensitive to the magnitude of the statistical threshold, with a better representation of surface O_3 achieved using a lower threshold.

1. Introduction

During polar spring, elevated levels of tropospheric bromine, referred to as "bromine explosion events" have been detected over both the Arctic and Antarctic (e.g., Barrie et al., 1988; Frieß et al., 2004; Oltmans et al., 1989; Richter et al., 1998). These bromine explosions drive boundary layer ozone depletion events (ODEs), where ozone (O_3) rapidly decreases from background mixing ratios to levels near zero (e.g., Bottenheim & Chan, 2006; Halfacre et al., 2014; Jones et al., 2006; Wessel et al., 1998). During ODEs halogens become the main tropospheric oxidant, impacting the lifetimes of Arctic pollutants (Bloss et al.,

2010; Evans et al., 2003) and increasing the deposition and biological uptake of elemental mercury (Gao et al., 2022; Holmes et al., 2006; Schroeder et al., 1998; Stephens et al., 2012). The underlying process resulting in bromine explosion events is connected to sea ice and thus is susceptible to the influence of climate change in polar regions (Pratt, 2019). However, there are currently multiple approaches for representing bromine explosion events in global models.

Similar to reactions that occur in the stratosphere, O_3 loss catalyzed by brominated species in the troposphere occurs via reactions between atomic bromine (Br) and bromine monoxide (BrO):

$$Br + O_3 \rightarrow BrO + O_2 \quad (1.1)$$

$$BrO + BrO \rightarrow 2Br + O_2 \quad (1.2)$$

Through gaseous and heterogeneous reactions, the bromine radicals cycle among the family of inorganic bromine compounds (Br_y = BrO + Br + 2×Br_2 + BrCl + BrI + $BrNO_3$, + $BrNO_2$ + HBr + HOBr) (Finlayson-Pitts, 2010; Saiz-Lopez & von Glasow, 2012; Simpson et al., 2015). Chlorine (Custard et al., 2017; Foster et al., 2001; Keil & Shepson, 2006; Liao et al., 2014) and iodine (Mahajan et al., 2010; Raso et al., 2017) containing compounds have been observed during polar spring, which can increase the catalytic efficiency of ozone loss. However, detection of iodine over the Arctic has been inconsistent and chlorine is less efficient at depleting O_3 due to competing reactivity with methane and hydrocarbons (Saiz-Lopez et al., 2012; Thompson et al., 2015).

Bromine explosion events are supplied by aqueous (aq) bromide ions (Br^-) from sea salt and converted into gas phase bromine through heterogeneous reaction on polar surfaces (e.g., sea ice or saline snow). Hypobromous acid (HOBr), formed from BrO:

$$BrO + HO_2 \rightarrow HOBr + O_2 \quad (1.3)$$

converts Br^- (aq) into gaseous molecular bromine (Br_2):

$$HOBr + Br^-(\text{aq}) + H^+(\text{aq}) \rightarrow H_2O + Br_2 \quad (1.4)$$

The produced Br_2 rapidly photolyzes to reform Br:

$$Br_2 + \text{hv} \rightarrow 2Br \quad (1.5)$$

which feeds back into the Br_y family and the formation of HOBr. Reaction 1.4 is considered to be the main pathway for bromine explosion events, and multiple saline surfaces have been considered for this heterogeneous process (Fan & Jacob, 1992; Simpson et al., 2007; Wennberg, 1999).

These surfaces include: sea ice, the continental saline snowpack (Cao et al., 2014; Foster et al., 2001; Pratt et al., 2013), frost flowers (T. L. Zhao et al., 2008), and sea salt aerosols generated by wind-driven blowing snow (Frey et al., 2020; Huang et al., 2018). The saline surfaces used to model the release of Br_2 are typically either sea ice and continental snowpack (Falk & Sinnhuber, 2018; Fernandez et al., 2019; Herrmann et al., 2021; Toyota et al., 2011) or sea salt aerosols from blowing snow (Huang et al., 2020; Yang et al., 2005, 2010; X. Zhao et al., 2016). Two recent modeling efforts have also represented bromine explosion events using a combination of snowpack and blowing snow source mechanisms (Marelle et al., 2021; Swanson et al., 2022). In both mechanisms, the Br^- in sea water is frozen in sea ice and taken up by the snowpack. However, blowing snow processes occur under high wind conditions, while snowpack related processes are typically associated with low wind and a stable boundary layer (Jones et al., 2009; Peterson et al., 2015; Swanson et al., 2020). While Marelle et al. (2021) found that bromine emitted by blowing snow had a minor impact on surface O_3 simulations relative to snowpack, other studies have been able to capture ODEs using only blowing snow sources (Huang et al., 2020; Yang et al., 2010). Furthermore, Yang et al. (2020) demonstrated that two models using similar bromine emissions schemes produced dissimilar Br_y and O_3 fields, reflecting the sensitivity of these simulations to differences in the modeled partitioning and resulting deposition of Br_y species.

In the present study, we develop emission estimates of Br_2 over the Arctic based on retrievals of BrO from the Ozone Monitoring Instrument (OMI) onboard NASA's Aura satellite. Levels of Br_y can be inferred from observations of BrO, and modeling studies frequently use satellite-based tropospheric columns of BrO to assess the performance of bromine explosion simulations (Herrmann et al., 2021; Huang et al., 2020; Toyota et al., 2011; Yang et al., 2010; X. Zhao et al., 2016). Satellite-based studies have frequently associated bromine explosion events with blowing snow conditions (Begoin et al., 2010; Blechschmidt et al., 2016; Choi et al., 2018), but ground-based studies have proposed that the bromine enhancements under shallow boundary layer conditions may not be detectable from space-based instruments (Sihler et al., 2012). Enhanced vertical columns of BrO associated with bromine explosion events were first detected by the Global Ozone Monitoring Experiment (GOME) satellite instrument (Chance, 1998; Richter et al., 1998; Wagner & Platt, 1998). In present day, multiple satellite instruments provide column retrievals of BrO with daily, global coverage (Seo et al., 2019; Sihler et al., 2012; Suleiman et al., 2019; Theys et al., 2011). The long-term record of BrO column retrievals has been used to connect increasing amounts of Arctic BrO to the increasing relative amount of first year to multiyear sea ice (Bougoudis et al., 2020; Hollwedel et al., 2004) and have been used to train an artificial neural network representation of tro-

pospheric columns (Bougoudis et al., 2022).

We interpret OMI retrievals of BrO using the GEOS-Chem chemical mechanism, coupled to the NASA Goddard Earth Observing System (GEOS) Earth system model. Section 2 provides a description of the employed model setup and instrumental measurements. The model setup was designed to be similar to the near-real time GEOS Composition Forecast (GEOS-CF, v1.0; Keller et al., 2021) system to facilitate the application of the results of this study in future efforts within the Global Modeling and Assimilation Office (GMAO). Additionally, Huang et al. (2020) and Swanson et al. (2022) have developed mechanisms for blowing snow and snowpack sources of bromine explosion events for the GEOS-Chem code, allowing for the availability of different approaches for representing polar bromine emissions within one chemical mechanism. Ground-based retrievals of BrO retrieved over Harestua, Norway are used to assess the vertical distribution of BrO in base model runs, while the performance of simulations with an Arctic bromine source are evaluated with measurements of BrO and O_3 collected by instruments onboard ice-tethered buoys and measurements of O_3 from coastal monitoring stations.

In section 3.1, we describe how the model is used to isolate tropospheric hotspots of BrO from OMI column retrievals over the Arctic with a threshold approach similar to past satellite-based studies (Bougoudis et al., 2020; Choi et al., 2018; Hollwedel et al., 2004; Seo et al., 2020; Theys et al., 2011). Due to the catalytic nature of these emissions, our preliminary efforts are focused on developing a lower-limit estimate. In section 3.2, we estimate the associated Br_2 flux that needs to be included to simulate the tropospheric hotspots. These fluxes are implemented in the model where elevated BrO signals are detected, agnostic of proximity to sea ice or continental tundra. The resulting simulations are evaluated with respect to observations of BrO, and the impact of the added bromine on surface O_3 simulations is assessed in section 3.3. Conclusions are provided in section 4.

2. Model and Measurement Descriptions

2.1. Model Setup

In this study, version 12.0.1 of the GEOS-Chem chemical mechanism (http://www.geos-chem.org) was run as a chemical module coupled to the NASA Goddard Earth Observing System (GEOS) Earth system model, as described by Long et al. (2015) and Hu et al. (2018). Simulations were conducted in replay mode (Orbe et al., 2017) using meteorological fields from the Modern-Era Retrospective Analysis for Research and Applications version 2 reanalysis (Gelaro et al., 2017; Global Modeling And Assimilation Office & Pawson, Steven, 2015). Ozone fields were free-running and calculated within GEOS-Chem rather than nudging the stratospheric ozone to the reanalysis ozone fields as is done for GEOS-CF (Knowland et al., 2022). All simulations were performed at a cubed sphere c90 horizontal resolution (nominally, 1° latitude × 1.25° longitude) with 72 levels from the surface layer up to 0.01 hPa.

The GEOS-Chem mechanism employs a detailed representation of HO_x-NO_x-VOC-ozone-halogen-aerosol chemistry (Bey et al., 2001). The halogen mechanism in GEOS-Chem v12.0.1 includes interactive chlorine, bromine, and iodine chemistry with gas phase and heterogeneous reactions (Sherwen et al., 2016). The bromine chemical mechanism is described by Schmidt et al. (2016) for the troposphere and by Eastham et al. (2014) for the stratosphere. Chen et al. (2017) introduced the reaction between HOBr and dissolved SO_2 (S(IV) = $HSO_3^- + SO_3^{2-}$) on cloud droplets that reduces the tropospheric loading of Br_y. Following Schmidt et al. (2016), the bromine source from sea salt aerosols was not included in our simulations, since this source results in unrealistically high BrO in the marine boundary layer. Thus, the main source of tropospheric Br_y in our simulations is from photodecomposition of CH_2Br_2 and $CHBr_3$.

Simulations were conducted with the fully coupled tropospheric and stratospheric chemical mechanism (Eastham et al., 2014) with the revisions described by Knowland et al. (2022). Briefly, the updates to the GEOS-Chem mechanism applied here include: kinetic rate constants and photolysis cross sections follow the recommendations from the 2015 Jet Propulsion Lab (JPL) kinetic evaluation (Burkholder et al., 2015), and surface boundary conditions for ozone depleting substances are defined by the WMO 2018 baseline scenario (Carpenter et al., 2018). Family transport of Br_y and inorganic chlorine species has been implemented to eliminate spurious maxima in the inorganic halogen families (e.g., Douglass et al., 2004). Additionally, in accordance with the Global Modeling Initiative (GMI) chemical mechanism (Douglass et al., 2004; Strahan et al., 2007), three heterogeneous reactions that produce BrCl have been turned off for stratospheric aerosols (Knowland et al., 2022). While simulations of BrO were not specifically evaluated in past GEOS-Chem studies with stratospheric chemistry, the stratospheric loading of bromine species was determined in Knowland et al. (2022) to be in agreement with the recommended values provided by Engel et al. (2018).

Our base simulation, presented in section 3, were run for January 2008 through December 2012. The model was spun-up as a free-running system for 9 years, starting in 1999 (see section 4 of Knowland et al. (2022), in order to distribute updates throughout the stratosphere. The final spin-up year replayed to MERRA-2 meteorology in order to have realistic atmospheric composition distributions for the specific years of interest. Two additional simulations are conducted with Arctic bromine emissions (section 3.3), where emissions of Br_2 are added using the Harvard-NASA Emissions Component (HEMCO; Keller et al., 2014).

2.2. Ozone Monitoring Instrument (OMI)

We use OMI retrievals to estimate Arctic emissions associated with bromine explosion events within the GEOS-Chem mechanism. OMI is an ultraviolet-visible, nadir viewing spectrometer onboard the NASA Aura satellite (Levelt et al., 2006). The Aura satellite was launched in July 2004 in a sun-synchronous, polar orbit with an equatorial crossing time of 13:45 in the ascending node.

The OMI swath width is 2600 km with a 13 × 24 km^2 spatial resolution at the center of the swath. Beginning in June 2007, a partial blockage impacts radiances collected by specific detector rows, referred to as the row anomaly (Schenkeveld et al., 2017).

The primary OMI product used in this study is the version 3.0.5 retrieval of BrO (Suleiman et al., 2019). This retrieval uses a wavelength fitting window of 319 – 347.5 nm and BrO cross sections measured at 228 K by Wilmouth et al. (1999). Vertical column densities (VCD) of BrO are determined from observed slant path through the atmosphere using a wavelength and albedo dependent air mass factor (AMF) that is calculated prior to spectral fitting. Slant column densities (SCD) and VCDs of BrO are calculated following spectral fitting of BrO, Ring scattering, O_3, nitrogen dioxide (NO_2), formaldehyde (CH_2O), chlorine dioxide (OClO), and sulfur dioxide (SO_2). Additional OMI data included in our analysis are stratospheric column NO_2 from the NASA column NO_2 product (OMNO2; Bucsela et al., 2013; Krotkov et al., 2017), cloud pressure from the rotational Raman scattering product (OMCLDRR; Vasilkov et al., 2008), and total column ozone and surface reflectivity at 331 nm from the NASA product based on the total ozone mapping spectrometer (TOMS) algorithm (OMTO3; McPeters et al., 2008).

Traditionally, AMFs are used to account for scattering along the satellite-observed path through the atmosphere and convert SCDs of trace gases to VCDs:

$$\mathrm{VCD} = \frac{\mathrm{SCD}}{\mathrm{AMF}} \quad (2.1)$$

Since the OMI retrieval of BrO applies AMFs prior to spectral fitting, an effective AMF is provided from the ratio of OMI BrO SCD/VCD (AMF^{OMI}). This AMF uses a mostly stratospheric a priori profile of BrO, and the sensitivity of the OMI retrieval to the BrO signal is partially dependent on the profile shape of the absorbing trace gas with the satellite instrument generally less sensitive to BrO in the lower troposphere (Suleiman et al., 2019). Thus, when there are significant amounts of BrO in the lower troposphere, such as during bromine explosion events, the OMI retrieval will underestimate the VCD of BrO and is accounted for following Choi et al. (2018).

For comparison to GEOS-Chem output, OMI data from each Aura overpass is averaged within a 1° latitude × 1° longitude grid. Retrievals are filtered to remove observations affected by the row anomaly and collected at solar zenith angles (SZA) greater than 80°. AMFs are calculated from GEOS-Chem profiles of BrO sampled at the OMI overpass time (AMF^{GC}) using scattering weight profiles prepared by Choi et al. (2012) with the Linearized Discrete Ordinate Radiative Transfer (LIDORT) model (Spurr et al., 2001). Since mixing ratios of tropospheric BrO are relatively low in GEOS-Chem version 12.0.1 (shown in section 3.1), the value of AMF^{GC} is similar to AMF^{OMI}, and the impact

of differences in the OMI and GEOS-Chem profiles of BrO on the analysis presented in section 3.1 is negligible. For analysis of tropospheric hotspots of BrO, OMI data is filtered using additional criteria and tropospheric AMF corrections are determined following Choi et al. (2018), as described in section 3.1.

2.3. Ground-Based Measurements of BrO over Harestua

GEOS-Chem modeled stratospheric and tropospheric columns of BrO are compared to ground-based retrievals over Harestua, Norway (60°N, 11°E) collected using zenith-sky ultraviolet-visible absorption spectroscopy (Hendrick et al., 2007, 2009). The Harestua station is part of the Network of the Detection of Atmospheric Composition Change (NDACC). A complete description of the instrument setup and BrO retrieval algorithm is given by Hendrick et al. (2007) with updates described in Choi et al. (2018). Slant column densities of BrO are retrieved using the differential optical absorption spectroscopy (DOAS; Platt & Stutz, 2008) technique at twilight hours. The DOAS retrieval algorithm uses the 336 – 359 nm wavelength fitting window with BrO cross sections from Fleischmann et al. (2004) and includes spectral fitting of BrO, the Ring effect, O_3, NO_2, O_2-O_2 collision complex, and OClO.

Values of SCDs of BrO are collected at high SZAs (80°, 85°, and 90°). Vertical profiles and VCDs of BrO are determined from the twilight measurements using the Optimal Estimation Method (OEM, Rodgers, 2000). Sunset profiles of BrO are converted to 13:15 local time using a stacked photochemical box model. This model also allows for the rapid variation of BrO in twilight hours to be accounted in the radiative transfer simulations associated to the profile retrieval (Hendrick et al., 2007, 2009).

Hourly GEOS-Chem output at 60°N, 11°E is interpolated over time to 13:15 local time for comparison to retrieved tropospheric and stratospheric columns collected between 2008 and 2011. In accordance with Hendrick et al. (2007), columns are filtered to only include observations collected between 15 February and 31 October each year, except for 2011 where separated tropospheric and stratospheric retrievals are only available through June. Errors associated with the ground-based VCDs, shown in section 3.1, are calculated based on the root sum of squares combination of the random and systematic errors.

2.4. Autonomous, Ice-Tethered Buoy Measurements

OMI-based detections and simulations of elevated bromine are evaluated using measurements of BrO and O_3 collected during four deployments of autonomous, ice-tethered buoys (O-Buoys) (Knepp et al., 2010). Data is publicly available through the National Science Foundation (NSF) Arctic Data Center (Simpson et al., 2009). Columns of BrO were retrieved from multi-axis differential optical absorption spectroscopy (MAX-DOAS) instruments (Carlson et al., 2010; Peterson et al., 2015), and surface mixing ratios of O_3 were measured by a UV-absorption sensor (Halfacre et al., 2014; Knepp et al., 2010). Springtime measurements of BrO were collected in 2011 by O-Buoys 2 and 3 and in 2012

by O-Buoys 4 and 6. Coincident measurements of O_3 with BrO are available for O-Buoy 2 and 4 deployments, while coincident measurements are sparse during O-Buoy 3 and 6 deployments. The mean locations of these measurements are shown in Figure 1 along with the location of the Harestua (section 2.3, shown as a square) and three coastal ozone stations (section 2.5, shown as triangles).

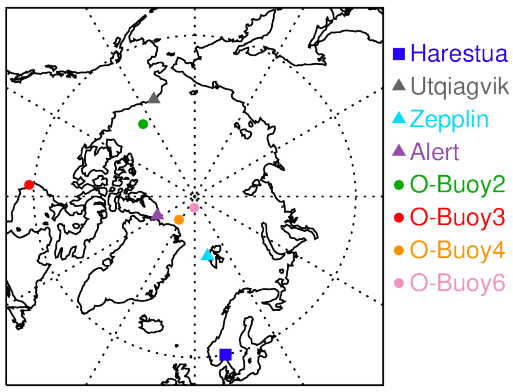

Figure 1. Locations of Harestua (Norway), Utqiagvik (Alaska, USA), Zeppelin (Svalbard, Norway), and Alert (Nunavut, Canada) measurement stations, and the mean locations of the O-Buoy deployments.

The MAX-DOAS instrument collects profiles of BrO from the surface to 4 km through the optimal estimation procedure (Frieß et al., 2006; Peterson et al., 2015). Peterson et al. (2015) determined the MAX-DOAS measurements are most sensitive to BrO signals that originate in a near surface layer, between the surface and 200 m, and in an aloft layer, between 200 m and 2000 m. The sensitivity to a priori information is reduced if the retrieval is represented as columns of BrO in the lowest 200 m above the surface (BrO^{200m}) and in the lower troposphere (BrO^{LT}), between the surface and 2000 m. The retrievals are filtered to only included data where the degrees of freedom for the signal in the near surface layer is > 0.7 and in the aloft layer is > 0.5 (Simpson et al., 2017). For comparison to OMI-based and simulated columns of BrO, only MAX-DOAS observations collected at SZAs $< 80°$ are included in our study.

Hourly output of surface layer O_3 and profiles of BrO from GEOS-Chem simulations are sampled along the O-Buoy tracks at the closest time to each MAX-DOAS measurement. Columns of BrO^{200m} and BrO^{LT} are determined from modeled profiles of BrO following the method presented by Swanson et al. (2022). For each time step along the buoy track, partial columns of modeled BrO are calculated along the vertical resolution of the MAX-DOAS averaging kernels. The resulting profile of partial columns are scaled according using the mean averaging kernel sensitivity for BrO^{200m} and BrO^{LT}, where the averaging kernel sensitivities are near unity at the surface and less than 0.5 respectively above 200 m and 2000 m, as described by Swanson et al. (2022). Each set of scaled partial columns are summed from 0 to 4 km and averaged per day (SZA

$< 80°$) to provide modeled BrO^{200m} and BrO^{LT}.

2.5. Station Ozone Measurements

Surface ozone simulations are evaluated using ground-level, in situ measurements collected at three coastal stations (see Figure 1) that detect springtime ODEs. Measurements from Utqiagvik, Alaska, USA (71.3°N, 156.7°W) are available from the NOAA Global Monitoring Laboratory (McClure-Begley et al., 2014; Oltmans & Levy, 1994). The ozone record from the Zeppelin Observatory (78.9°N, 11.9°E) near Ny-Alesund, Norway is provided by Norwegian Institute for Air Research (Platt et al., 2021). Lastly, measurements from Alert, Nunavut, Canada (82.5°N, 62.5°W) are available from the Canadian Air and Precipitation Monitoring Network (CAPMoN).

3. Results and Discussion

A method for isolating OMI columns of BrO (BrO^{OMI}) that are likely associated with Arctic bromine explosion events is presented in section 3.1. A bias threshold is defined based on the difference between OMI and GEOS-Chem columns of BrO observed outside of regions influenced by bromine explosion events. Values of BrO^{OMI} larger than the bias threshold are identified as tropospheric hotspots of BrO (hereafter, BrO^{TH}) and represent a lower limit estimate for the magnitude of bromine explosion events. In section 3.2, the process for estimating emissions of Br_2 from OMI-based BrO^{TH} and incorporating this flux into the model is described. In section 3.3, simulations of Arctic bromine are presented and are evaluated with respect to OMI and ice-tethered buoy observations of BrO. Additionally, the impact of the added emissions on modeled surface O_3 is presented, and the sensitivity of the simulations to the bias threshold is assessed.

3.1. Detecting Hotspots of BrO

Globally, the GEOS-Chem (v12.0.1) modeled BrO column (BrO^{GC}) is systematically biased low with respect to BrO^{OMI} (Figure 2). The black and blue solid lines in Figure 2 are the respective means of BrO^{OMI} and BrO^{GC} as a function of latitude, averaged over 2008 to 2012. The grey shading represents the standard deviation about the mean in BrO^{OMI}, while the blue dashed lines represent the standard deviation in BrO^{GC}. For all results presented in section 3.1, hourly model output is interpolated to the OMI overpass time.

Throughout the tropics and midlatitudes, modeled BrO^{GC} is about 1×10^{13} molecules cm^{-2} lower than retrieved BrO^{OMI}. Larger differences between BrO^{GC} (blue) and BrO^{OMI} (black) are observed at high latitudes where OMI detects polar emissions of bromine. The majority of BrO^{GC} resides in the stratospheric column, as indicated by the orange line in Figure 2, and larger values of BrO^{GC} are simulated over northern high latitudes (i.e., upper blue dashed line in Figure 2) due to amplifications of the stratospheric column during boreal spring. As discussed in section 2.2, the OMI retrieval of BrO vertical columns assumes a mostly stratospheric a priori profile (Suleiman et al., 2019). Since GEOS-Chem simulates relatively low contributions from the

tropospheric column, shown in purple, the difference between OMI a priori and modeled BrO profiles has a negligible impact on the comparison between BrO^{OMI} and BrO^{GC}.

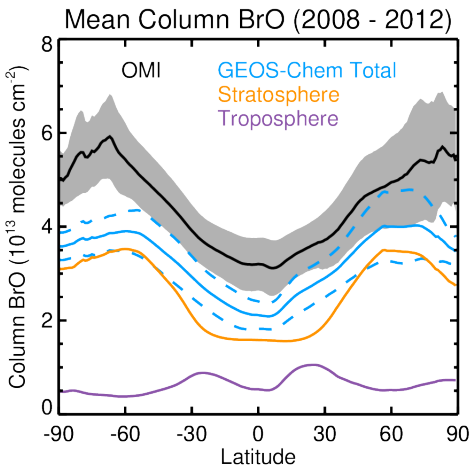

Figure 2. OMI retrieved and GEOS-Chem simulated column BrO averaged over 2008 – 2012. The black line and grey shaded region are the mean and standard deviation of OMI column BrO. The blue solid and dashed lines are the mean and standard deviation, respectively, of GEOS-Chem column BrO at OMI overpass time. The stratospheric and tropospheric components of the GEOS-Chem column are shown as orange and purple lines, respectively.

We use ground-based observations over Harestua, Norway (61°N) to evaluate the vertical distribution of GEOS-Chem columns of BrO at the closest grid-box to Harestua for 2008 through 2011 (Figure 3 and S1). As described in section 2.3, the twilight retrieval of the ground-based instrument allows for the separation of the column into tropospheric and stratospheric components, which is not available from nadir-viewing satellite instruments. Previous studies have reported close agreement between BrO^{OMI} and ground-based total (i.e., stratospheric + tropospheric) column BrO over Harestua, with a mean bias of $0.1 \pm 0.7 \times 10^{13}$ molecules cm^{-2} (Choi et al., 2018; Suleiman et al., 2019), indicating that the Harestua observations are a useful proxy for investigating the origin of the bias shown in Figure 2.

The seasonal trend in the stratospheric column of BrO observed by the ground-based instrument is captured by the GEOS-Chem simulation, as demonstrated for 2008 in Figure 3 (see supporting information Figure S1 for 2009 – 2011 time series). Overall, the model represents the stratospheric column of BrO over Harestua well with respect to ground-based observations (Figure 3a). For the full time series, the correlation coefficient (r) between the two stratospheric columns is 0.69, and the mean and standard deviation of the bias is $-0.3 \pm 0.5 \times 10^{13}$ molecules cm^{-2}, with the modeled columns lower than reported by the

ground-based retrievals (Figure 3c). The modeled tropospheric column of BrO is poorly correlated with the ground-based observations and has a mean bias of $-0.7 \pm 0.6 \times 10^{13}$ molecules cm^{-2} (Figure 3d). Overall, the total bias in BrO^{GC} is $-1.0 \pm 0.6 \times 10^{13}$ molecules cm^{-2} relative to the ground-based observations, consistent with the bias relative to BrO^{OMI} (Figure 2). Thus, the majority of the low bias in BrO^{GC} is of tropospheric origin over Harestua.

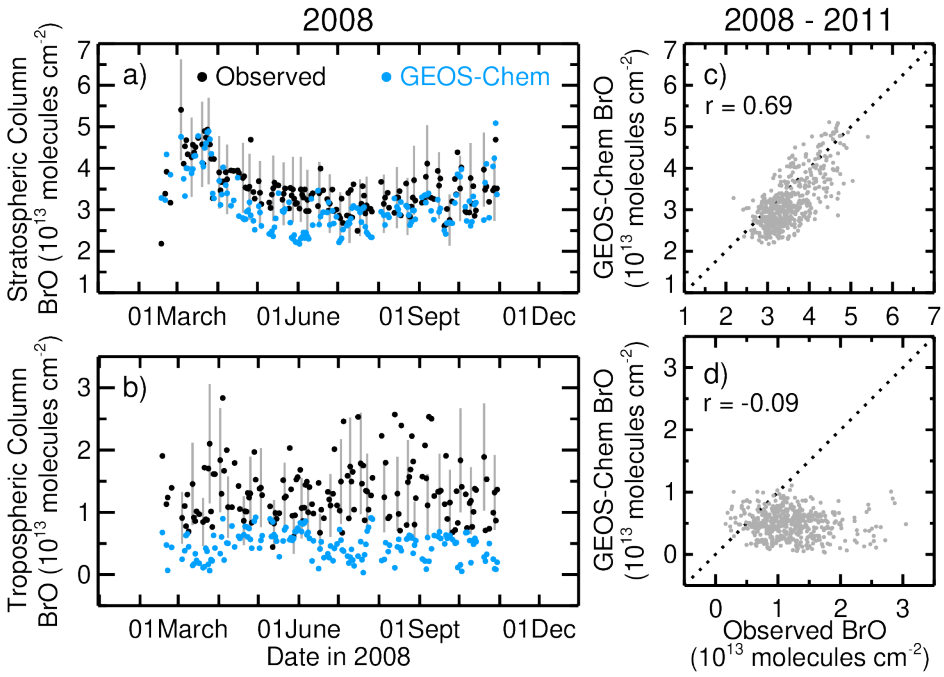

Figure 3. Modeled and measured stratospheric (top row) and tropospheric (bottom row) columns of BrO over Harestua, Norway for 2008 (a and b) and for 2008-2011 (c and d). (a and b) GEOS-Chem modeled columns are in blue, ground-based measurements are in black, and the uncertainty associated with the ground-based observations are included for every fifth measurement in grey. (c and d) In both panels, the 1 to 1 line is represented as a dotted line and the correlation coefficients between the two datasets are provided.

The tropospheric column of BrO shown in Figures 2 and 3 is lower than reported by previous GEOS-Chem studies (Schmidt et al., 2016; Sherwen et al., 2016). The tropospheric bromine source from open ocean sea salt aerosols is not included in our simulations, because GEOS-Chem studies report that sea salt debromination results in significant overestimations in tropospheric column BrO in comparison to observations (Schmidt et al., 2016; Zhu et al., 2019). While open ocean sea salt aerosols are a significant source of bromine in the marine boundary layer, this source is not sufficient to drive the low O_3 episodes observed during polar spring (Huang et al., 2020; Yang et al., 2020). Furthermore, the addition of the HOBr + S(IV) reaction to GEOS-Chem by Chen et al.

(2017) increases the wet deposition of Br_y species, reducing tropospheric Br_y by 50% relative to the bromine mechanism presented by Schmidt et al. (2016). Revisions of the tropospheric halogen mechanism after version 12.0.1 have improved the representation of sea salt debromination through updates to the tropospheric sinks and heterogenous recycling of Br_y (Wang et al., 2021; Zhu et al., 2019). Consequently, in the present study we do not attribute the entire difference between BrO^{OMI} and BrO^{GC} to polar processes, and we introduce a method for estimating polar emissions that is adaptable to later revisions in the GEOS-Chem mechanism.

We evaluate the distribution of BrO^{OMI} and BrO^{GC} differences outside of polar regions to minimize the impact of modeled biases in the stratosphere and tropospheric background on our interpretation of bromine explosion signals. Histograms of the difference between BrO^{OMI} and BrO^{GC} within non-polar (50°S and 50°N) and Arctic (50°N and 90°N) latitude bands are shown in Figure 4. For 2008 through 2012, the mean non-polar difference between BrO^{OMI} and BrO^{GC} is 1.0×10^{13} molecules cm^{-2}, with a normal distribution and a standard deviation ( ) of 0.6×10^{13} molecules cm^{-2}. The non-polar mean bias + 3 is 2.7×10^{13} molecules cm^{-2} (red dashed line in Figure 4) and is used as a statistical bias threshold ($_{BIAS}$) to identify incidents of BrO^{TH}. This value is larger than 99.7% of the difference between OMI and GEOS-Chem columns of BrO observed in the tropics and midlatitudes. Since background values of tropospheric column BrO have been proposed that range from 0.5 to 3×10^{13} molecules cm^{-2} (e.g., Hendrick et al., 2007; Schofield et al., 2004; Van Roozendael et al., 2002), if the majority of the BrO^{OMI} – BrO^{GC} bias resides in the troposphere, the use of 2.7×10^{13} molecules cm^{-2} for $_{BIAS}$ also effectively accounts for the upper-limit of background tropospheric columns reported by previous studies. Thus, the + 3 bias threshold primarily used in our study represents a lower limit for the occurrences of BrO^{TH}. In section 3.3, a + 2 bias threshold (2.1×10^{13} molecules cm^{-2}, yellow line in Figure 4) is considered to assess the sensitivity of surface ozone and estimated polar bromine emission to the choice of a bias threshold.

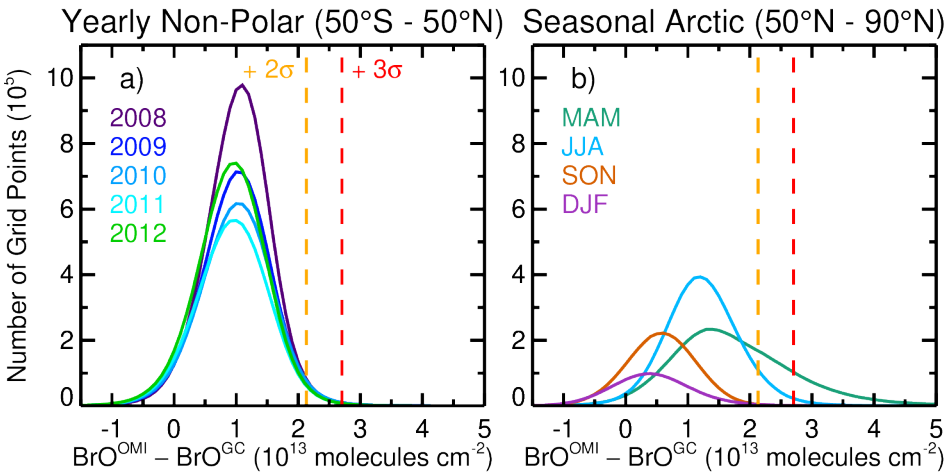

Figure 4. Histograms of the difference in column $BrO^{OMI} - BrO^{GC}$. Model grid points are binned and counted for every 0.1×10^{13} molecules cm^{-2}. Panel (a) shows the yearly distribution between latitudes of 50°S and 50°N, and panel (b) shows the seasonal distribution for all years between 50°N and 90°N. The dashed lines in both panels are the non-polar mean difference + 2 (yellow) and + 3 (red).

Our threshold method is similar to approaches taken by other studies that explored bromine explosion events using satellite retrievals and a stratospheric climatology of BrO (Bougoudis et al., 2020; Choi et al., 2018; Theys et al., 2011). The mode of the $BrO^{OMI} - BrO^{GC}$ distributions poleward of 50°N are within ± 1 of the non-polar mean difference for each season (Figure 4b), indicating that analysis presented in Figure 4a is valid for the Arctic region. For spring months (March, April, and May) shown in green in Figure 4b, there are more detections of BrO^{OMI} that exceed both the +3 and +2 thresholds than in the other seasons, reflecting the detection of springtime bromine explosion events. The + 3 threshold primarily used in our study represents a lower limit for the occurrences of BrO^{TH} over the Arctic, since some elevations in BrO^{OMI} below this value are likely also associated with polar processes. In section 3.3, a + 2 threshold (2.1×10^{13} molecules cm^{-2}) is considered to assess the sensitivity of surface ozone and calculated polar bromine emission to the choice of $_{BIAS}$. This lower threshold increases the detection of BrO^{TH} during spring and summer (blue in Figure 4b) months over the Arctic but is still larger than 98% of the bias observed over non-polar regions.

Columns of BrO retrieved by OMI and modeled by GEOS-Chem are shown for three days in April 2008 in Figure 5, characterizing the day-to-day variations of satellite and modeled BrO. For latitudes poleward of 50°N and for each day between 01 February and 30 June, regions where the difference between BrO^{OMI} and BrO^{GC} exceed $_{BIAS}$ (+ 3) are identified as BrO^{TH}, as presented for the case study period of 04 to 06 April 2008 (third row of Figure 5).

During conditions with elevated tropospheric BrO, the BrO^{OMI} retrieval underestimates the VCD due to the use of a mostly stratospheric a priori profiles of BrO in the AMF calculation (section 2.2). For each grid cell flagged as a tropospheric hotspot, AMF^{GC} is calculated using the overpass GEOS-Chem profile of BrO according to section 2.2. The magnitude of BrO^{TH} is determined using the tropospheric residual method (e.g., Theys et al., 2011; Wagner & Platt, 1998):

$$BrO^{TH} = \frac{SCD^{OMI} - (BrO^{GC} + \sigma_{BIAS}) \times AMF^{GC}}{AMF^{TROP}} \quad (3.1)$$

with tropospheric air mass factors (AMF^{TROP}) prepared by Choi et al. (2012) using a BrO a priori profile based on aircraft measurements collected during the Arctic Research of the Composition of the Troposphere from Aircraft and Satellite (ARCTAS) campaign. To avoid conditions that contribute to large uncertainties in AMF^{TROP}, the filtering procedure presented in Choi et al. (2018) is followed such that only retrievals where the SZA $< 80°$, viewing zenith angle $< 65°$, and OMI reflectivity at 331 nm > 0.6 are included. Additionally, regions influenced by optically thick clouds are removed where the difference between the surface and OMI detected cloud pressures are > 100 hPa (Vasilkov et al., 2010).

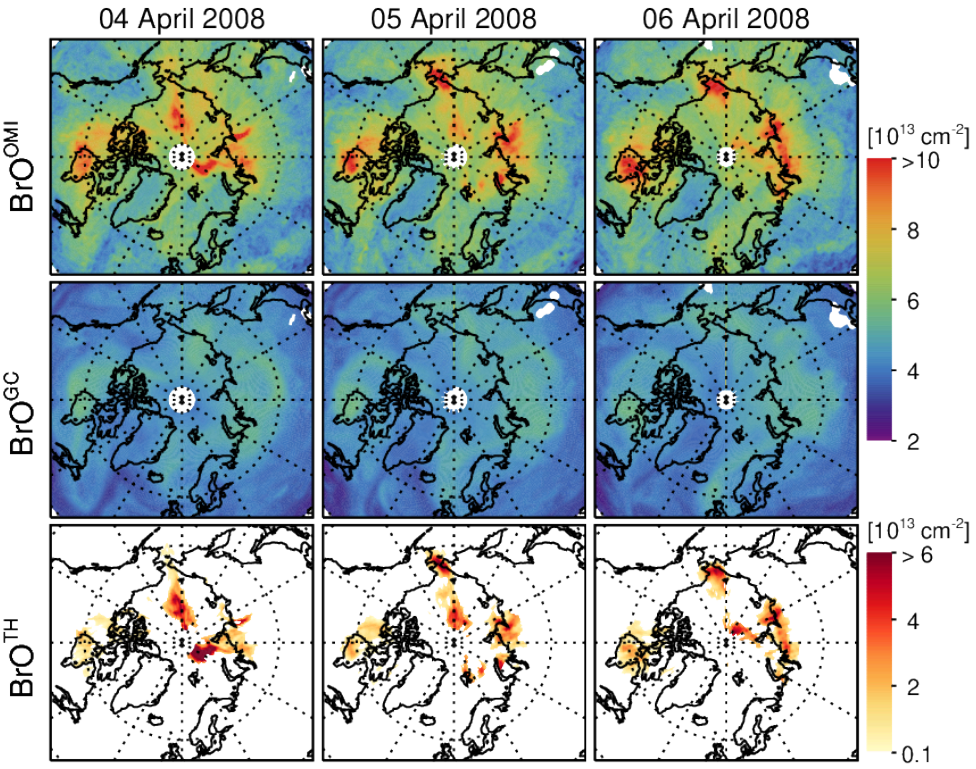

Figure 5. Column BrO over the northern hemisphere for 04 – 06 April 2008. The first row is retrieved BrO^{OMI}, the second row is modeled BrO^{GC} sampled at OMI overpass time and averaged per day if multiple overpasses are present, and the third row is BrO^{TH} calculated according to equation 3.1.

During boreal spring, spatial gradients in Arctic total column BrO^{GC} are driven by variations in the stratospheric column, as high values of column BrO are frequently associated with low tropopause heights, where stratospheric BrO compresses to lower altitudes (Begoin et al., 2010; Salawitch et al., 2010; Seo et al., 2020; Theys et al., 2011). As demonstrated in Figure 5, some enhancements in BrO^{OMI} with respect to the zonal mean are also reflected in broad features simulated in BrO^{GC}. For instance, portions of the hotspots in BrO^{OMI} over northern Canada are attributed to enhancements in the stratosphere rather than BrO^{TH}. Consequently, accurately accounting for variations in the stratospheric column, due to dynamics and chemical partitioning, is required to isolate regions of BrO^{TH}.

Close correlation between GEOS-Chem simulated and ground-based observed stratospheric columns are demonstrated over Harestua (Figure 3c). Description and evaluation of the GEOS-Chem stratospheric mechanism and chemical fields related to BrO are provided by Eastham et al. (2014) and Knowland et al. (2022). The daytime stratospheric column of BrO has a positive correlation with total column O_3 due to similar responses in both columns to stratospheric dynamics (Salawitch et al., 2010; Theys et al., 2009). Our simulations are replayed to MERRA-2 meteorological fields with free-running ozone (section 2.1). During boreal spring (March to May) over the years 2008 to 2012, simulations of total column O_3 poleward of 50°N capture the magnitude and variability observed by OMI (Table S1). The mean and standard deviation of the relative bias between modeled and OMI column O_3 is – 1.5 ± 3.1 %, and correlation coefficient between the two columns is 0.97, reflecting the model's ability to capture the influence of stratospheric dynamics on column BrO.

The stratospheric partitioning of Br_y species into BrO is highly sensitive to mixing ratios of NO_2 via the termolecular reaction forming $BrONO_2$ (Sioris et al., 2006; Theys et al., 2009). In the northern hemisphere, stratospheric NO_2 increases from March to May, resulting in a decrease in daytime stratospheric BrO as more Br_y is partitioned into $BrONO_2$, as reflected in the stratospheric column of BrO over Harestua (Figure 3a and S1). GEOS-Chem captures the magnitude and seasonality of OMI stratospheric column NO_2 with a mean relative bias of 0.4 ± 7.1% and r = 0.98 (Table S1). However, uncertainties in modeling the stratospheric column remain (e.g., Wales et al., 2021), further motivating our use of a statistical threshold for interpreting the BrO^{OMI} – BrO^{GC} residuals.

3.2. Calculating Arctic Flux of Br_2

For each year, BrO^{TH} is calculated according to equation (3.1) for 01 February through 01 July and latitudes poleward of 50°N. While most bromine explo-

sion events occur during March through May, February and June are included to capture the beginning and end of the season. Daily flux of Br_2 (F_{Br2}) is calculated with a 1° × 1° horizontal resolution based on the values of BrO^{TH}. The emitted Br_2 rapidly photolyzes during the day (reaction 1.5) and feeds into the Br and BrO (BrO_x) cycle (reactions 1.1 and 1.2). Throughout the day, the added bromine distributes among Br_y compounds, and Br_y is eventually removed from the troposphere via wet and dry deposition of HBr, HOBr, and $BrONO_2$. To accurately represent the observed values of BrO^{TH} in the model, we must account for how much of the emitted Br_2 will partition into Br_y species other than BrO and how long the added Br_y will remain in the system.

We estimate the column of Br_y associated with each value of BrO^{TH} using the modeled ratio of tropospheric columns of BrO:Br_y ($_{Bry}$). From the base GEOS-Chem simulation without Arctic bromine emissions (section 3.1), $_{Bry}$ at OMI overpass time has a linear relationship with SZA over latitudes poleward of 50°N, SZAs < 80°, and OMI reflectivity > 0.6, as shown in supporting information Figure S2a. For each value of BrO^{TH}, $_{Bry}$ is calculated as a linear function of the overpass SZA, where at a SZA of 40° the value of $_{Bry}$ is about 0.3, and at a SZA of 70° the value of $_{Bry}$ is closer to 0.5.

From preliminary tuning experiments conducted for the 2008 season, we found that: (1) modeled $_{Bry}$ increases as BrO^{GC} increases with respect to the base simulation (BrO^{GC}, Figure S2b), and (2) the added bromine remains in the system for longer than day, resulting in significant over representations of BrO^{TH} later in the season. From Figure S2b, for $BrO^{GC} > 4 \times 10^{13}$ molecules cm^{-2}, $_{Bry}$ increases by 0.14 with respect to linearly calculated values (Figure S2a). Thus, for the remainder of the study, $_{Bry}$ is assumed to be 0.14 larger than estimated from the SZA linear fit for values of BrO^{TH} larger than 4×10^{13} molecules cm^{-2} (Figure S2b):

$$0.187 + \mathrm{SZA}\ ,\ \ \&\ \mathrm{BrO}\hat{}\ \hat{}13 \tag{3.2}$$

To represent the impact of the tropospheric lifetime of Br_y on F_{Br2} calculations, the total mass of bromine associated with columns of BrO^{TH} is calculated over the Arctic (M_t) using $_{Bry}$ for each day (t):

$$M_t = \sum \left(\frac{\mathrm{BrO}^{\mathrm{TH}}}{\chi_{\mathrm{Bry}}} \times\ mass_{\mathrm{conv}} \times\ \mathrm{SA}_{\mathrm{grid}} \right) \tag{3.3}$$

where SA_{grid} is the surface area of each 1° × 1° grid box. Since the bromine added by F_{Br2} remains in the system for longer than a day, only a fraction of M_t is due to new emissions. Based on preliminary simulations, approximately 50%

of the added bromine is located between the surface and 500 m in altitude. Consequently, the median e-folding lifetime of Br_y integrated below 500 m ($_{500m}$) is used to approximate how long the added bromine remains in the system, and the springtime median modeled value of $_{500m}$ is 3 days over the relevant study area (i.e., latitudes > 50°N and OMI reflectivity > 0.6). The fraction of M_t that is due to fresh emissions (M_{frac}) is estimated daily according to:

$$M_{\text{frac}} = \frac{M_t - M_{t-1} \times e^{-\frac{1\ day}{t_{500m}}}}{M_t} \quad (3.4)$$

For each value of BrO^{TH}, F_{Br2} is calculated according to:

$$F_{Br_2} = \frac{BrO^{TH}}{\chi_{Bry}} \times\ mass_{\text{conv}} \times M_{\text{frac}} \quad (3.5)$$

where BrO^{TH} is temporally and spatially resolved and M_{frac} is a daily value. Emissions are applied over one day (UTC) with no assumed diurnal variation. However, the tropospheric lifetime of Br_y is not normally distributed and is highly variable in both time and space, with lifetimes generally increasing with increasing altitude. Since a single value is used for $_{500m}$, this method will not capture temporal and spatial gradients in the lifetime.

Between 2008 and 2012, the mean emission of bromine determined from equation 3.5 is 4.3 Gg Br year^{-1}, with values ranging between 3.1 and 6.1 Gg Br year^{-1}. Over regions where the calculation of F_{Br2} is not zero, the mean and standard deviation of F_{Br2} is 1.1 ± 1.0 × 10^8 molecules cm^{-2} s^{-1} with values as high as 18 × 10^8 molecules cm^{-2} s^{-1}. Our OMI hotspot-based yearly emissions of Arctic bromine are significantly lower than the values reported by the Fernandez et al. (2019) bottom-up study, where the bromine release from sea ice and heterogeneous recycling over the snowpack was estimated to be 270 Gg Br year^{-1} over the Arctic, with 127 Gg Br emitted during boreal spring. However, our fluxes are similar in magnitude to the 0.7 and 12 × 10^8 molecules cm^{-2} s^{-1} range reported by Custard et al. (2017) based on measurements of Br_2 collected above an illuminated snowpack.

3.3. Simulating Arctic Emissions of Bromine

Following the initial sensitivity simulation described in section 3.2 to determine F_{Br2}, two simulations with an Arctic source of bromine (hereafter referred to "ABr") are defined by equation (3.5) with BrO^{TH} calculated using a value of 2.7 × 10^{13} molecules cm^{-2} (+ 3 , Figure 4) and using a value of 2.7 × 10^{13} molecules cm^{-2} (+ 2) for $_{BIAS}$ in equation (3.1). ABr_3 simulations were conducted each year for 01 February to 01 July, and the difference in BrO^{GC} between the base and ABr_3 simulation (BrO^{GC}) are shown in Figure 6 at OMI overpass time for the same three days illustrated in Figure 5. The local spatial features of

BrO^{TH} are generally well captured by BrO^{GC}. While simulations of BrO^{GC} are initially low with respect to BrO^{TH} along the Russian coast on 06 April 2008, high values of BrO^{TH} are captured well in this area on the following days (not shown). Also, during 04 – 06 April 2008, the large values of BrO^{GC} over Hudson Bay in northern Canada are partially the result of F_{Br2} released earlier in the season and are associated with high values of BrO^{OMI} with similar spatial pattern. However, due to larger values of BrO^{GC}, relatively small amounts of BrO^{OMI} are attributed to BrO^{TH} over this region. Finally, upon application of F_{Br2} in GEOS-Chem, isolated but large decreases in surface layer O_3 are modeled, with values on 04 April 2008 reaching up to 21 ppb over northern Canada, a 55% decrease relative to base simulation (last row in Figure 6).

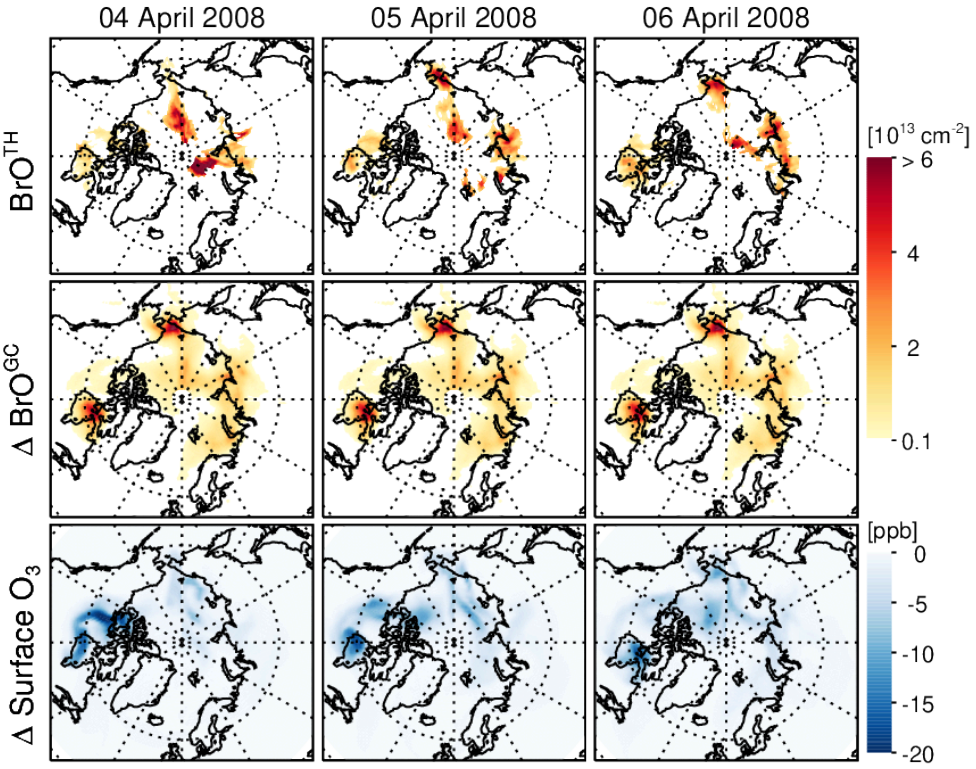

Figure 6. Column BrO and surface O_3 over the northern hemisphere for 04 – 06 April 2008. The first row is BrO^{TH} as shown in Figure 5, the second row is BrO^{GC} sampled at OMI overpass time and averaged per day if multiple overpasses are present, and the third row is the decrease in surface layer O_3 for ABr_3 simulations.

We assess the ability of our ABr_3 emission scheme to capture the OMI-based BrO^{TH} signals by comparing the total, daily mass of bromine contained in BrO^{TH} and BrO^{GC} respectively shown as black and red lines in Figure 7 for 2008 – 2012. Since the mass shown in Figure 7 is only for that contained in

BrO (i.e., $_{\mathrm{Bry}}$ is not considered), the total mass of bromine associated with the hotspots (equation 3.3) is larger than shown. Because the daily mass changes by orders of magnitude during the spring, we determine the normalized mean bias (NMB):

$$NMB = \frac{\sum(\Delta \mathrm{BrO}^{\mathrm{GC}} - BrO^{\mathrm{TH}})}{\sum \mathrm{BrO}^{\mathrm{TH}}} \quad (3.6)$$

over 01 March through 31 May for all five years. The simulated total mass of $\mathrm{BrO}^{\mathrm{GC}}$ captures the daily magnitude and variability of $\mathrm{BrO}^{\mathrm{TH}}$ with a NMB of 15% and r = 0.92. The skill at simulating springtime daily mass of $\mathrm{BrO}^{\mathrm{TH}}$ varies greatly from year-to-year, with NMB values ranging from – 3% up to + 50% and 0.72 r 0.96. Periods where $\mathrm{BrO}^{\mathrm{GC}}$ overrepresents $\mathrm{BrO}^{\mathrm{TH}}$ are typically accompanied by increases in the mass of $\mathrm{Br_y}$ larger than the mass of $\mathrm{M_t}$ calculated by equation (3.3), suggesting that our treatment of the lifetime of $\mathrm{Br_y}$ in equation (3.4) contributes to the high values of $\mathrm{BrO}^{\mathrm{GC}}$.

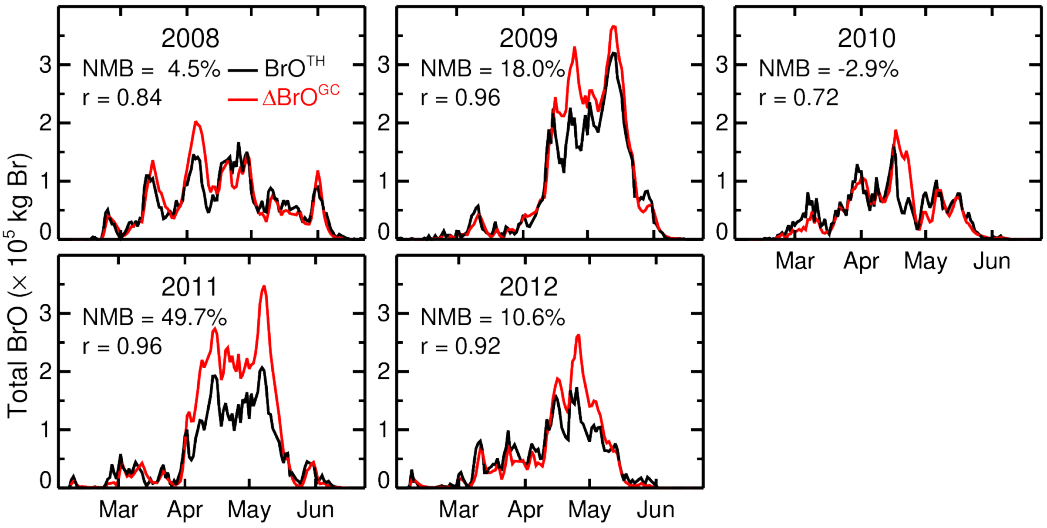

Figure 7. Daily mass of bromine in $\mathrm{BrO}^{\mathrm{TH}}$ (black) and $\mathrm{BrO}^{\mathrm{GC}}$ (red) from ABr_3 simulations for 01 February – 01 July, 2008 to 2012. Values for the NMB and correlation coefficients are provided each year for spring months (i.e., 01 March – 31 May).

To determine the sensitivity of our simulations to the magnitude of $_{\mathrm{BIAS}}$ used to calculate $\mathrm{BrO}^{\mathrm{TH}}$ (equation 3.1), an experiment is conducted using a threshold that is the non-polar mean bias + 2 (yellow dashed line in Figure 4). This is a 0.6×10^{13} molecules cm^{-2} reduction in $_{\mathrm{BIAS}}$ with respect to the + 3 threshold used in the ABr_3 simulation. Values of $\mathrm{BrO}^{\mathrm{TH}}$ and $\mathrm{F_{Br2}}$ (equation 3.5) are re-calculated with the lower threshold and implemented for 01 February through 01

July 2012 only. We refer to the resulting simulation as "ABr_2 ", and the yearly emissions for the ABr_2 scenario is 9.5 Gg Br year^{-1}, double the 2012 emissions (4.3 Gg Br year^{-1}) calculated for the ABr_3 simulation that year. The daily mass of bromine contained in BrO^{TH} and BrO^{GC} are in good agreement with NMB = 8% and r = 0.93. These values are similar to the ABr_3 2012 results shown in Figure 7 (NMB = 11% and r = 0.92), indicating that the method introduced in section 3.2 performs consistently with larger quantities of BrO^{TH}.

Our detection of elevated bromine is assessed by comparing OMI-based columns of BrO^{TH} to retrievals of BrO columns in the lower troposphere, BrO^{LT}, collected by MAX-DOAS instruments onboard ice-tethered O-Buoys (section 2.4). Since the ABr_2 simulation was conducted only for 2012, O-Buoy tracks for this year are highlighted in Figures 8 and Table 1, with 2011 tracks in supporting information Figure S3 and Table S2. Daily mean BrO^{TH} for both thresholds of $_{BIAS}$ are shown along the 2012 O-Buoy tracks in Figure 8a and 8e, where missing points of BrO^{TH} are due to filtering of the OMI data, as described in sections 2.2 and 3.1.

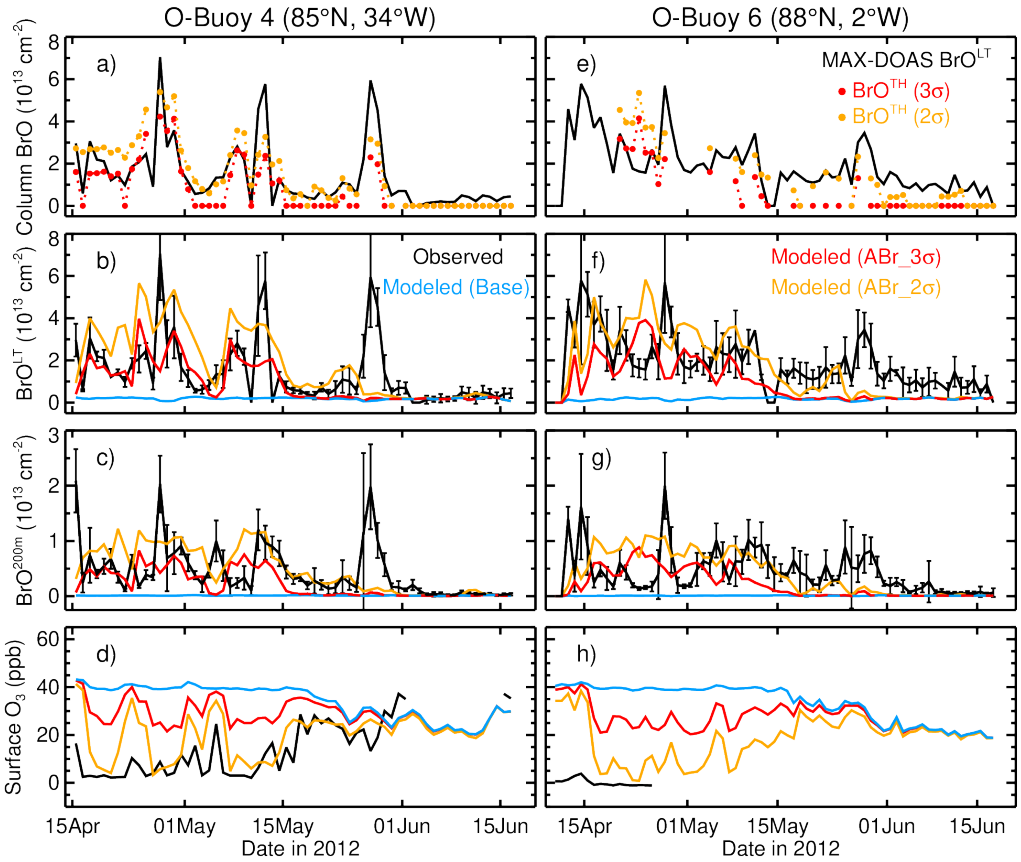

Figure 8. Daily mean observations and modeled parameters sampled along the

2012 (a – d) O-Buoy 4 and (e – g) O-Buoy 6 tracks. In panels (a and e), points are OMI-based values of BrO^{TH} along the buoy tracks and black lines are MAX-DOAS BrO^{LT}. In the remaining panels, black lines are buoy-based observations, and the blue, red, and yellow lines are respectively the simulations for the base, ABr_3 , and ABr_2 scenarios. BrO^{LT} is shown in panels (b and f), BrO^{200m} in panels (c and g), and surface O_3 in panels (d and h). All BrO columns are daytime (SZA $< 80°$), daily means, and error bars represent the standard deviation about the MAX-DOAS daily mean.

Estimations of BrO^{TH} are well correlated with daytime, daily means of MAX-DOAS BrO^{LT} with r = 0.73 during 2012 for both values of $_{BIAS}$. Similarly, the correlation for the 2011 and 2012 time periods is r = 0.66 (Table S2); however, correlation weakens over Hudson Bay during March 2011 (Figure S3e). The overall good correlation (r = 0.66) between BrO^{TH} and the observed BrO^{LT} indicates that despite the persistent background bias between BrO^{OMI} and BrO^{GC}, our method for calculating BrO^{TH} is able to isolate BrO signals associated with the lower troposphere. While lowering the value of $_{BIAS}$ does not significantly impact the correlation between BrO^{TH} and the buoy-based retrievals, the lower threshold reduces the number of negative detections along all four tracks.

As discussed in section 2.4, the MAX-DOAS retrievals of BrO^{LT} and BrO^{200m} are respectively most sensitive to the lowest 2 km and 200 m above the surface. Modeled profiles of BrO are scaled according to the retrieval sensitivity (Swanson et al., 2022) to calculate modeled columns of BrO^{LT} (Figure 8b and 8f) and BrO^{200m} (Figure 8c and 8g). Simulated columns of BrO^{LT} are less correlated with MAX-DOAS retrievals than observed for the BrO^{TH} analysis, with r values of 0.37 and 0.45 for the ABr_3 and ABr_2 scenarios, respectively (Table 1). As demonstrated with Figure 7, these simulations perform well with respect to BrO^{TH} when assessed over the whole study region but as shown in Figure 6, do not always capture the magnitude of local features. The mean bias between the ABr_2 and MAX-DOAS columns is lower than the ABr_3 simulations with a mean and standard deviation of $0.04 \pm 1.60 \times 10^{13}$ molecules cm^{-2} for BrO^{TH} columns (Table 1), demonstrating that the ABr_2 simulation generally captures the magnitude of BrO along these buoy tracks, albeit with a slight overestimate of BrO between 15 April and 15 May 2012 and an underrepresentation of detected peaks in BrO later in the season (Figure 8).

Table 1. Mean bias, standard deviation, and correlation coefficient between daytime, daily mean BrO columns produced by the present study (i.e., from equation 3.1 and ABr simulations) and those retrieved from a MAX-DOAS instrument during O-Buoy deployments in 2012.

OMI and model-based columns	MAX-DOAS column	Mean bias ($\times 10^{13}$ molecules cm^{-2})	r
BrO^{TH} (3)	BrO^{LT}	– 0.8 ± 1.0	
BrO^{LT} (ABr_3)	BrO^{LT}	– 0.8 ± 1.4	

OMI and model-based columns	MAX-DOAS column	Mean bias ($\times 10^{13}$ molecules cm^{-2})	r
BrO^{200m} (ABr_3)	BrO^{200m}	– 0.2 ± 0.5	
BrO^{TH} (2)	BrO^{LT}	− 0.08 ± 1.1	
BrO^{LT} (ABr_2)	BrO^{LT}	± 1.60	
BrO^{200m} (ABr_2)	BrO^{200m}	± 0.500	

Along each buoy track, there are periods where surface layer O_3 mixing ratios in the ABr_3 simulations (shown in red in Figures 8d and 8g) decrease by over 10 ppb (about 25%) with respect to the base simulation (shown in blue). These decreases in surface O_3 do not exceed 20 ppb (i.e., 50%), and the near-zero mixing ratios measured during the O-Buoy tracks are not captured by the ABr_3 simulation (Figures 8d for O-Buoy 4 and Figure S3d for O-Buoy 2). For the ABr_2 scenario (shown in yellow), periods of O_3 mixing ratios < 10 ppb are simulated over both O-Buoy 4 and 6, and measurements are well represented over the O-Buoy 4, demonstrating the sensitivity of ozone simulations to the choice of $_{BIAS}$ in interpreting BrO^{TH}. However, periods in April 2012 where observed ozone depletion episodes are captured are associated with times when local BrO^{200m} is overestimated by the ABr_2 simulation (Figure 8c).

To further investigate the impact of the Arctic bromine simulations, we sample model output at the locations of three coastal stations that monitor surface O_3 (section 2.5, Figure 1). The daily mean observations for February through June 2012 from these stations are shown in black in Figure 9, and simulations of surface-layer O_3 sampled at the closest grid-box to these three locations are shown for the base (blue), ABr_3 (red), and ABr_2 (yellow) simulations. Similar panels are shown for 2008 – 2011 in Figure S4.

Generally, all simulations capture background mixing ratios of O_3 during February and June, with the exception of a low model bias over the Zeppelin station during June (Figure 9). In April and May 2012, the application of F_{Br2} results in lower values of surface O_3 simulated over all three stations, and an ozone depletion episode is captured over Alert in late April. However, for 2008 through 2012 the impact of the ABr_3 emissions on surface O_3 over the coastal stations is generally small (Figures 9 and S4). Consistent with results over O-Buoys in the Arctic Ocean (Figure 8), more ozone loss is captured in the ABr_2 than in the ABr_3 simulation. However, decreasing $_{BIAS}$ for the detection of BrO^{TH} has only a minor impact on surface layer O_3 over coastal stations during March 2012, and the low ozone events over Utqiagvik are still not fully captured in the ABr_2 scenario (Figure 9).

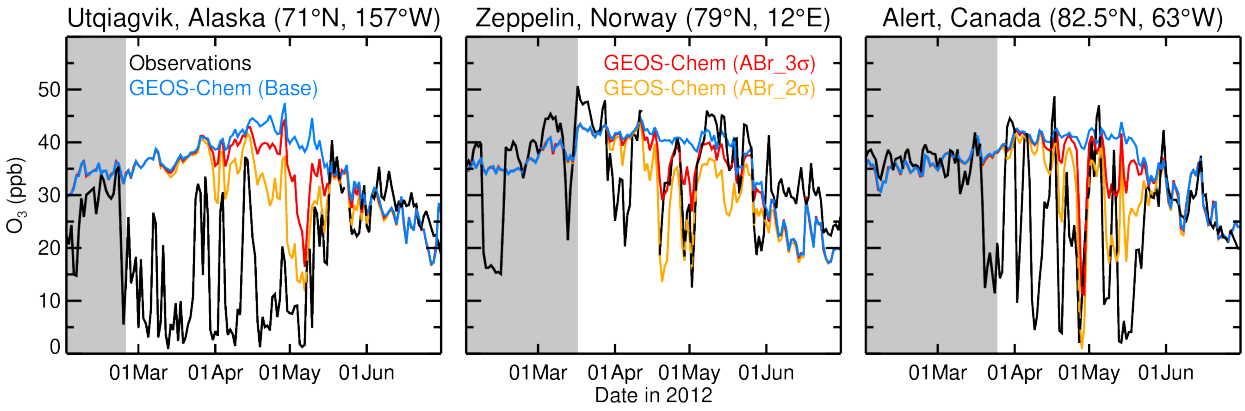

Figure 9. Daily mean modeled and observed surface O_3 over three stations during spring 2012. Ozone observations are shown in black, the base GEOS-Chem simulation is shown in blue, ABr_3 simulation is in red, and the ABr_2 threshold sensitivity scenario in yellow. The grey shading in each panel indicates time periods where SZAs $> 80°$ at local noon. The locations of these stations are shown in Figure 1.

The grey shading in Figure 9 indicates when retrievals of BrO^{OMI} are not available over each station due to daytime SZAs $> 80°$. Over regions where OMI retrievals of BrO are unavailable, either due to filtering criteria or missing overpasses, values of BrO^{TH} are treated as zero for the day. Because of the 80° SZA limit, OMI observations are available only as far north as 72°N on 01 March and 85°N on 01 April 2012. Thus, if during March 2012 the low ozone episode observed over Alert, Canada (82.5°N) is due to local bromine chemistry, or if the low ozone over Utqiagvik, Alaska (71°N) was transported from higher latitudes, the associated emissions would be missing in our satellite-based approach.

To evaluate the impact of F_{Br2} over the whole study region, monthly mean column BrO and surface-layer O_3 statistics are shown in Figure 10 for the 2012 ABr_3 simulation. Similar figures are shown in supporting information for the earlier years (Figures S5 – S8), and in Figure 11 for the 2012 ABr_2 simulation. From the analysis presented in Figure 7, the total mass of daily BrO^{GC} over the study region is well correlated with, but with a slight high bias with respect to, detected BrO^{TH} ($r = 0.92$; NMB = 11%). This high bias is seen near the North Pole in April monthly mean BrO^{GC} in both Figures 10 and 11. Also, the BrO^{GC} fields have lost some of the detail present in the BrO^{TH} monthly mean map, particularly along the northern Alaskan and Siberian coastlines in Figure 11, potentially contributing to the high bias in surface ozone over Utqiagvik (Figure 9).

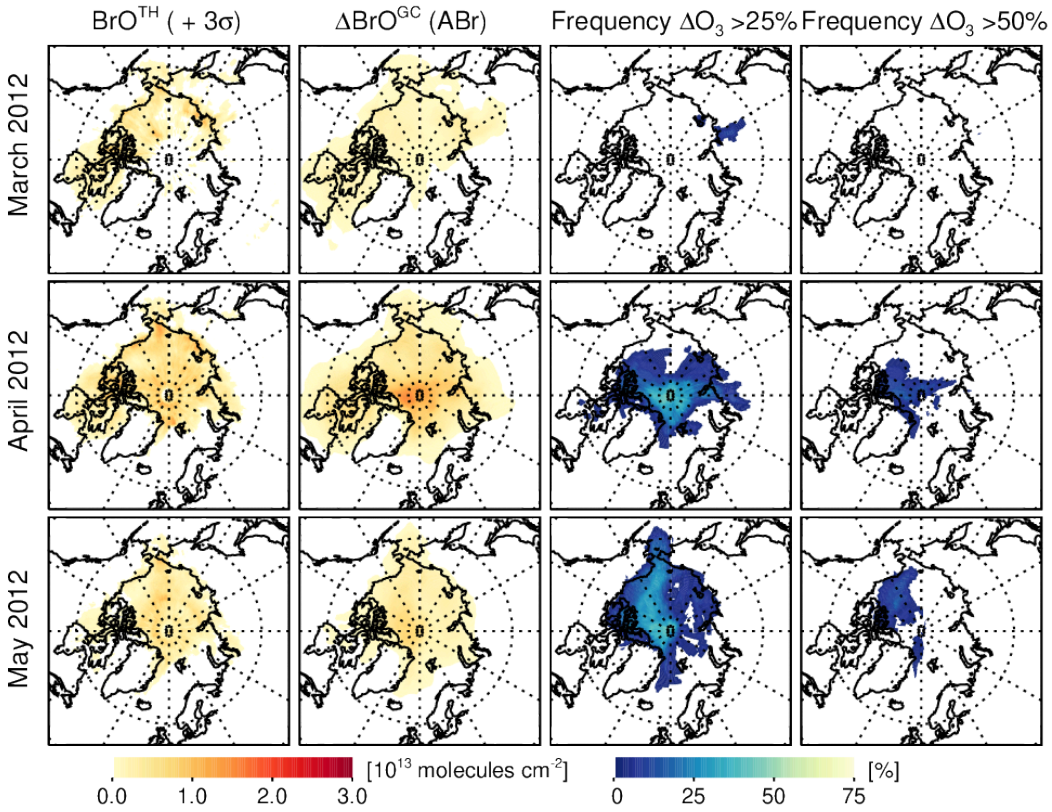

Figure 10. Monthly column BrO and surface layer O_3 statistics for 2012. The first and second columns respectively are monthly mean BrO^{TH} and BrO^{GC} for the ABr_3 scenario. The third and fourth columns show how frequently there are large (> 25 and 50%, respectively) decreases in modeled surface layer ozone between base and ABr_3 simulations.

For latitudes poleward of 60°N, the monthly mean decreases in ABr_3 surface ozone (O_3) relative to the base simulation are 0.6, 7.2, and 8.5% for March, April, and May 2012, respectively. For the ABr_2 sensitivity scenario, these values are 1.4, 18.5, and 21.6%. As demonstrated in Figure 6, the application of a lower-limit estimate to the polar flux of Br_2 results in isolated but large values of O_3 that are not captured by monthly mean calculations. In Figures 10 and 11, we highlight how frequently there are large decreases in surface O_3, defined as where O_3 is greater than 25 or 50%.

Overall, larger amounts of O_3 loss are simulated later in the season than in early spring, as seen over coastal stations (Figure 9). During March 2012, there are no events simulated where O_3 > 50% and infrequent events with O_3 > 25% for both scenarios. Monthly mean statistics for the 2008 – 2011 time periods (Figures S5 – S8), similarly demonstrate that periods of large O_3 loss

are infrequently modeled during March ABr_3 simulations. Additionally, there is interannual variability in the frequency of these events in late spring that reflects the variability in detected BrO^{TH} (Figure 7), with more frequent events detected in 2009 and 2011 than in 2008 and 2010. While in ABr_3 simulations, events where $O_3 > 50\%$ are relatively infrequent during April and May 2012, there are occurrences of $O_3 > 25\%$ over most of the Arctic Ocean during this period, with locations near the pole experiencing $O_3 > 25\%$ for roughly half of both months (Figure 10). During April and May 2012, occurrences of large O_3 from the ABr_2 simulation cover a greater surface area and last for more days (Figure 11) than in the ABr_3 simulation.

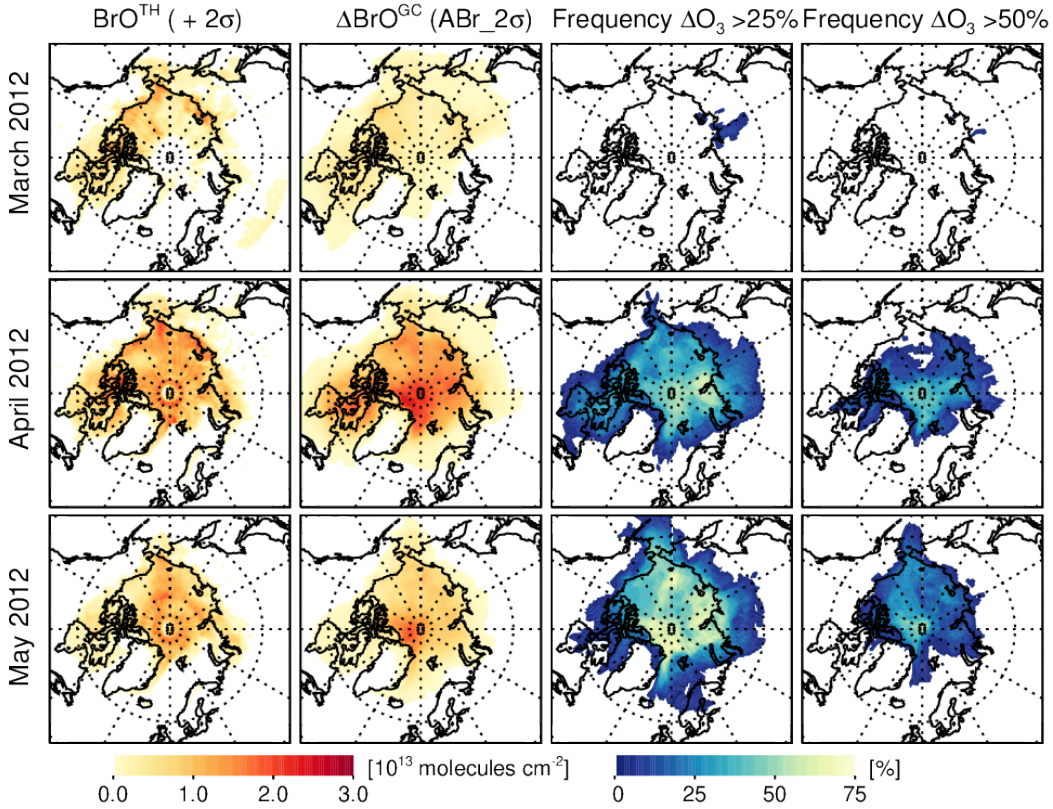

Figure 11. Same as Figure 10 but for the ABr_2 threshold sensitivity simulation.

4. Conclusions

We introduce a novel method for estimating emissions of Br_2 associated with bromine explosion events using OMI retrievals of column BrO (BrO^{OMI}) and the GEOS-Chem (v12.0.1) chemical mechanism. Profiles of BrO are simulated for 01 January 2008 – 31 December 2012 at c90 resolution by the GEOS general circulation model, coupled to the GEOS-Chem chemical module and replayed

to MERRA-2 meteorological reanalysis. These simulations are conducted with the full stratospheric and tropospheric GEOS-Chem mechanism that was recently evaluated in a similar GEOS setup (Knowland et al., 2022). We follow recommendations to not include the sea salt aerosol source of bromine in this version of GEOS-Chem (Schmidt et al., 2016); however, more recent versions of the mechanism have improved the representation of this source by updating the tropospheric sinks and heterogeneous uptake of bromine species (Wang et al., 2021; Zhu et al., 2019).

Modeled columns of BrO (BrO^{GC}) in base simulations without an Arctic bromine source are systematically lower than retrieved BrO^{OMI}. The mean and standard deviation ( ) of the difference in the two columns (BrO^{OMI} – BrO^{GC}) outside of regions impacted by polar bromine explosion events (i.e., 50°S – 50°N) is 1.0 ± 0.6 × 10^{13} molecules cm^{-2}. The stratospheric portion of BrO^{GC} is well correlated (r = 0.69) with ground-based retrievals of BrO over Harestua, Norway (61°N) with a mean bias of – 0.3 ± 0.5 × 10^{13} molecules cm^{-2}. Meanwhile, the tropospheric portion of BrO^{GC} is not correlated with the ground-based measurements (r = – 0.09) with a mean bias of – 0.7 ± 0.6 × 10^{13} molecules cm^{-2}. This indicates that most of the bias in BrO^{GC} over Harestua originates from the troposphere, consistent with the lack of a sea salt aerosol bromine source in our simulations.

A statistical threshold is used to isolate hotspots of BrO^{OMI} over the Arctic that are likely associated with springtime bromine explosion events. To account for modeled uncertainties in the stratospheric and background tropospheric column of BrO, the threshold was chosen to be the non-polar BrO^{OMI} – BrO^{GC} mean bias + 3 , 2.7 × 10^{13} molecules cm^{-2}. The resulting tropospheric hotspot columns of BrO (BrO^{TH}) represent a lower limit for the impact of polar emissions on BrO^{OMI} signals. A sensitivity study is conducted by reducing the bias threshold to the non-polar mean bias + 2 , 2.1 × 10^{13} molecules cm^{-2}. During 2011 and 2012, both values of BrO^{TH} (3 and 2 -based) are well correlated with lower tropospheric columns of BrO (BrO^{LT}) collected by MAX-DOAS instruments onboard ice-tethered buoys (r = 0.66).

Emissions of Br_2 are estimated for each day at the location of the detected BrO^{TH} using parameters calculated within GEOS-Chem to account for the partitioning of total inorganic bromine species (Br_y) into observable BrO and the median atmospheric lifetime of Br_y in the lowest 500 m. Since updates to the GEOS-Chem mechanism since version 12.0.1 may impact the Br_y partitioning and resulting lifetime within the model, these two parameters may be adjusted to adapt this emission scheme in future modeling efforts. The resulting Arctic bromine emissions are applied in the model for February through June over 2008 – 2012 using the 3 threshold (ABr_3) and over 2012 using the 2 threshold (ABr_2). Reducing the bias threshold in 2012 nearly doubles the calculated emissions with respect to ABr_3 simulations, demonstrating the sensitivity of these calculations to the removal of the background signal of BrO.

Overall, the increase in BrO^{GC} in Arctic bromine with respect to base simula-

tions (BrO^{GC}) captures the magnitude and daily variability of BrO^{TH}. For 2008 – 2012 ABr_3 simulations, the daily mass of bromine contained in BrO^{GC} and BrO^{TH} totaled over the study area are well correlated with each other (r = 0.92) with a normalized mean bias (NMB) of 15%. The skill at capturing BrO^{TH} is maintained for the 2012 ABr_2 simulation but varies per year within ABr_3 simulations with a NMB of – 2.9% (r = 0.72) found for the 2010 season and 49.7% (r = 0.96) for 2011. Over the Arctic Ocean buoy deployments in 2012, MAX-DOAS partial columns of BrO are better represented by ABr_2 than ABr_3 simulations, and both scenarios represent a significant improvement with respect to the base simulation.

Our lower limit estimate of Br_2 emissions, based on the + 3 threshold, results in modest decreases in surface O_3 mixing ratios during April and May months, with a mean 8% decrease simulated poleward of 60°N in 2012, and isolated decreases in surface $O_3 > 25$ and 50% are simulated over portions of the Arctic. For all years tested, only minor amounts of ozone loss are captured over the Arctic in March (0.6% in 2012), and ABr_3 simulations do not capture the low mixing ratios of O_3 measured at coastal stations. During April and May 2012, the ABr_2 emissions result in a mean 20% decrease in surface O_3 with respect to base simulations. Additionally, in ABr_2 simulations more frequent large relative decreases (> 50%) in surface O_3 are captured over the Arctic Ocean, and mixing ratios of surface layer O_3 are in closer agreement with coastal and buoy observations than in ABr_3 simulations. Despite the reduced threshold, only a minor impact on surface O_3 was captured in early spring.

The poor agreement with O_3 observations during early spring represents a limitation in our approach, in part due to high SZAs in early spring that limit OMI retrievals over the high Arctic. At present, our method for detecting polar emissions of bromine relies on amplifications in the column of BrO detectable by nadir-viewing satellite instruments. If there are periods where polar emissions produce columns of BrO that are small with respect to the variability in BrO^{OMI} – BrO^{GC} residual, these columns may not be separated from signals originating from the stratosphere or background troposphere. Furthermore, previous studies have found that satellite instrument may underestimate elevations in near-surface BrO under meteorological conditions associated with a stable boundary layer (Peterson et al., 2015; Sihler et al., 2012; Swanson et al., 2020).

Overall, our method for implementing polar emissions of bromine can reproduce satellite-based hotspots of BrO detected over the Arctic, with a greater impact on O_3 captured in late than in early spring. Due to the catalytic nature of bromine-mediated ozone depletion, near-surface ozone simulations are sensitive to how much of BrO^{OMI} is attributed to Arctic bromine emissions. The emission scheme presented in this paper relies on a long-term base simulation of BrO^{GC} that is mostly of stratospheric origin, while the use of a bias threshold primarily accounts for uncertainties in the background tropospheric column. The 2 bias threshold is a likely candidate for future investigations since the ABr_2 simulation produced realistic BrO partial columns with respect to MAX-DOAS

and improved surface-layer O_3 simulations with respect to coastal and Arctic Ocean observations. Additionally, more computationally efficient methods for removing the stratospheric signal from satellite-based retrievals of BrO (e.g., Sihler et al., 2012; Theys et al., 2009) would facilitate the incorporation of this emission scheme into long-term historical or near-real time simulations.

Acknowledgments, Samples, and Data

The source code for GEOS-Chem v12.0.1 is available at https://zenodo.org/record/1403144 (doi: 10.5281/zenodo.1403144). MERRA-2 reanalysis fields (doi: 10.5067/WWQSXQ8IVFW8) and OMI data (doi: 10.5067/Aura/OMI/DATA2006) are maintained by the Goddard Earth Sciences Data and Information Services Center (GES DISC). Column measurements of BrO retrieved over Harestua, Norway by UV/Vis Spectroscopy were obtained by Francois Hendrick Michel and Van Roozendael as part of the Network for Detection of Atmospheric Composition Chage (NDACC) and are available through the NDACC website (http://www.ndaccdemo.org/stations/harestua-norway). Measurements of BrO and O_3 collected by instruments onboard autonomous, ice-tethered buoys are maintained by the National Science Foundation (NSF) Arctic Data Center (https://doi.org/10.18739/A2WD4W). Surface ozone measurements are available at https://gml.noaa.gov/aftp/data/ozwv/SurfaceOzone/ for Utqiagvik and http://ebas.nilu.no/ for the Zeppelin station, and surface ozone data from Alert, Nunavut is provided by Environment and Climate Change Canada from the Canadian Air and Precipitation Monitoring Network (https://donnees.ec.gc.ca/data/air/monitor/monitoring-of-atmospheric-gases/ground-level-ozone/).

PAW was supported by the NASA Postdoctoral Program, administered by Universities Space Research Association (USRA). Resources supporting the GEOS coupled with GEOS-Chem model simulations were provided by the NASA Center for Climate Simulations (NCCS). KEK, CAK, and SP acknowledge support by the NASA Modeling, Analysis and Prediction (MAP) Program (Project manager David Considine). The authors thank William R. Simpson for his guidance in the usage of BrO measurements collected by MAX-DOAS instruments onboard ice-tethered buoys.

References

Barrie, L. A., Bottenheim, J. W., Schnell, R. C., Crutzen, P. J., & Rasmussen, R. A. (1988). Ozone destruction and photochemical reactions at polar sunrise in the lower Arctic atmosphere. *Nature*, *334*(6178), 138–141. https://doi.org/10.1038/334138a0Begoin, M., Richter, A., Weber, M., Kaleschke, L., Tian-Kunze, X., Stohl, A., et al. (2010). Satellite observations of long range transport of a large BrO plume in the Arctic. *Atmospheric Chemistry and Physics*, *10*(14), 6515–6526. https://doi.org/10.5194/acp-10-6515-2010Bey, I., Jacob, D. J., Yantosca, R. M., Logan, J. A., Field, B. D., Fiore, A. M., et al. (2001). Global modeling of tropospheric chemistry with assimilated meteorology: Model description and evaluation.

Journal of Geophysical Research: Atmospheres, *106*(D19), 23073–23095. https://doi.org/10.1029/2001JD000807Blechschmidt, A.-M., Richter, A., Burrows, J. P., Kaleschke, L., Strong, K., Theys, N., et al. (2016). An exemplary case of a bromine explosion event linked to cyclone development in the Arctic. *Atmospheric Chemistry and Physics*, *16*(3), 1773–1788. https://doi.org/10.5194/acp-16-1773-2016Bloss, W. J., Camredon, M., Lee, J. D., Heard, D. E., Plane, J. M. C., Saiz-Lopez, A., et al. (2010). Coupling of HOx, NOx and halogen chemistry in the antarctic boundary layer. *Atmospheric Chemistry and Physics*, *10*(21), 10187–10209. https://doi.org/10.5194/acp-10-10187-2010Bottenheim, J. W., & Chan, E. (2006). A trajectory study into the origin of spring time Arctic boundary layer ozone depletion. *Journal of Geophysical Research*, *111*(D19), D19301. https://doi.org/10.1029/2006JD007055Bougoudis, I., Blechschmidt, A.-M., Richter, A., Seo, S., Burrows, J. P., Theys, N., & Rinke, A. (2020). Long-term time series of Arctic tropospheric BrO derived from UV–VIS satellite remote sensing and its relation to first-year sea ice. *Atmospheric Chemistry and Physics*, *20*(20), 11869–11892. https://doi.org/10.5194/acp-20-11869-2020Bougoudis, I., Blechschmidt, A.-M., Richter, A., Seo, S., & Burrows, J. P. (2022). Simulating tropospheric BrO in the Arctic using an artificial neural network. *Atmospheric Environment*, *276*, 119032. https://doi.org/10.1016/j.atmosenv.2022.119032Bucsela, E. J., Krotkov, N. A., Celarier, E. A., Lamsal, L. N., Swartz, W. H., Bhartia, P. K., et al. (2013). A new stratospheric and tropospheric NO2 retrieval algorithm for nadir-viewing satellite instruments: applications to OMI. *Atmospheric Measurement Techniques*, *6*(10), 2607–2626. https://doi.org/10.5194/amt-6-2607-2013Burkholder, J. B., Sander, S. P., Abbatt, J., Barker, J. R., Huie, R. E., Kolb, C. E., et al. (2015). *Chemical Kinetics and Photochemical Data for Use in Atmospheric Studies, Evaluation Number 18*. Jet Propulsion Laboratory, Pasadena: Jet Propulsion Laboratory. Retrieved from http://jpldataeval.jpl.nasa.gov/Cao, L., Sihler, H., Platt, U., & Gutheil, E. (2014). Numerical analysis of the chemical kinetic mechanisms of ozone depletion and halogen release in the polar troposphere. *Atmospheric Chemistry and Physics*, *14*(7), 3771–3787. https://doi.org/10.5194/acp-14-3771-2014Carlson, D., Donohoue, D., Platt, U., & Simpson, W. R. (2010). A low power automated MAX-DOAS instrument for the Arctic and other remote unmanned locations. *Atmospheric Measurement Techniques*, *3*(2), 429–439. https://doi.org/10.5194/amt-3-429-2010Carpenter, L. J., Daniel, J. S., Fleming, E. L., Hanaoka, T., Hu, J., Ravishankara, A. R., et al. (2018). Scenarios and Information for Policymakers, Chapter 6. In *Scientific Assessment of Ozone Depletion: 2018*. Geneva, Switzerland: World Meteorological Organization.Chance, K. (1998). Analysis of BrO measurements from the Global Ozone Monitoring Experiment. *Geophysical Research Letters*, *25*(17), 3335–3338. https://doi.org/10.1029/98GL52359Chen, Q., Schmidt, J. A., Shah, V., Jaeglé, L., Sherwen, T., & Alexander, B. (2017). Sulfate production by reactive bromine: Implications for the global sulfur and reactive bromine budgets. *Geophysical Research Letters*, *44*(13), 7069–7078. https://doi.org/10.1002/2017GL073812Choi, S., Wang, Y., Salawitch, R. J.,

Canty, T., Joiner, J., Zeng, T., et al. (2012). Analysis of satellite-derived Arctic tropospheric BrO columns in conjunction with aircraft measurements during ARCTAS and ARCPAC. *Atmospheric Chemistry and Physics*, *12*(3), 1255–1285. https://doi.org/10.5194/acp-12-1255-2012Choi, S., Theys, N., Salawitch, R. J., Wales, P. A., Joiner, J., Canty, T. P., et al. (2018). Link Between Arctic Tropospheric BrO Explosion Observed From Space and Sea-Salt Aerosols From Blowing Snow Investigated Using Ozone Monitoring Instrument BrO Data and GEOS-5 Data Assimilation System. *Journal of Geophysical Research: Atmospheres*, *123*(13), 6954–6983. https://doi.org/10.1029/2017JD026889Custard, K. D., Raso, A. R. W., Shepson, P. B., Staebler, R. M., & Pratt, K. A. (2017). Production and Release of Molecular Bromine and Chlorine from the Arctic Coastal Snowpack. *ACS Earth and Space Chemistry*, *1*(3), 142–151. https://doi.org/10.1021/acsearthspacechem.7b00014Douglass, A. R., Stolarski, R. S., Strahan, S. E., & Connell, P. S. (2004). Radicals and reservoirs in the GMI chemistry and transport model: Comparison to measurements. *Journal of Geophysical Research*, *109*(D16), D16302. https://doi.org/10.1029/2004JD004632Eastham, S. D., Weisenstein, D. K., & Barrett, S. R. H. (2014). Development and evaluation of the unified tropospheric-stratospheric chemistry extension (UCX) for the global chemistry-transport model GEOS-Chem. *Atmospheric Environment*, *89*, 52–63. https://doi.org/10.1016/j.atmosenv.2014.02.001Engel, A., Rigby, M., Burkholder, J. B., Fernandez, R. P., Froidevaux, L., Hall, B. D., et al. (2018). Update on Ozone-Depleting Substances (ODSs) and Other Gases of Interest to the Montreal Protocol, Chapter 1. In *Scientific Assessment of Ozone Depletion: 2018, Global Ozone Research and Monitoring Project – Report No. 58*. Geneva, Switzerland: World Meteorological Organization.Evans, M. J., Jacob, D. J., Atlas, E., Cantrell, C. A., Eisele, F., Flocke, F., et al. (2003). Coupled evolution of BrO_x -ClO_x -HO_x -NO_x chemistry during bromine-catalyzed ozone depletion events in the arctic boundary layer. *Journal of Geophysical Research*, *108*(D4), 8368. https://doi.org/10.1029/2002JD002732Falk, S., & Sinnhuber, B. M. (2018). Polar boundary layer bromine explosion and ozone depletion events in the chemistry-climate model EMAC v2.52: Implementation and evaluation of AirSnow algorithm. *Geoscientific Model Development*, *11*(3), 1115–1131. https://doi.org/10.5194/gmd-11-1115-2018Fan, S.-M., & Jacob, D. J. (1992). Surface ozone depletion in Arctic spring sustained by bromine reactions on aerosols. *Nature*, *359*(6395), 522–524. https://doi.org/10.1038/359522a0Fernandez, R. P., Carmona-Balea, A., Cuevas, C. A., Barrera, J. A., Kinnison, D. E., Lamarque, J., et al. (2019). Modeling the Sources and Chemistry of Polar Tropospheric Halogens (Cl, Br, and I) Using the CAM-Chem Global Chemistry-Climate Model. *Journal of Advances in Modeling Earth Systems*, *11*(7), 2259–2289. https://doi.org/10.1029/2019MS001655Finlayson-Pitts, B. J. (2010). Halogens in the troposphere. *Analytical Chemistry*, *82*(3), 770–776. https://doi.org/10.1021/ac901478pFleischmann, O. C., Hartmann, M., Burrows, J. P., & Orphal, J. (2004). New ultraviolet absorption cross-sections of BrO at atmospheric temperatures measured by time-windowing Fourier trans-

form spectroscopy. *Journal of Photochemistry and Photobiology A: Chemistry*, *168*(1–2), 117–132. https://doi.org/10.1016/j.jphotochem.2004.03.026Foster, K. L., Plastridge, R. A., Bottenheim, J. W., Shepson, P. B., Finlayson-Pitts, B. J., & Spicer, C. W. (2001). The Role of Br $_2$ and BrCl in Surface Ozone Destruction at Polar Sunrise. *Science*, *291*(5503), 471–474. https://doi.org/10.1126/science.291.5503.471Frey, M. M., Norris, S. J., Brooks, I. M., Anderson, P. S., Nishimura, K., Yang, X., et al. (2020). First direct observation of sea salt aerosol production from blowing snow above sea ice. *Atmospheric Chemistry and Physics*, *20*(4), 2549–2578. https://doi.org/10.5194/acp-20-2549-2020Frieß, U., Hollwedel, J., König-Langlo, G., Wagner, T., & Platt, U. (2004). Dynamics and chemistry of tropospheric bromine explosion events in the Antarctic coastal region. *Journal of Geophysical Research: Atmospheres*, *109*(D6), n/a-n/a. https://doi.org/10.1029/2003JD004133Frieß, U., Monks, P. S., Remedios, J. J., Rozanov, A., Sinreich, R., Wagner, T., & Platt, U. (2006). MAX-DOAS O $_4$ measurements: A new technique to derive information on atmospheric aerosols: 2. Modeling studies. *Journal of Geophysical Research*, *111*(D14), D14203. https://doi.org/10.1029/2005JD006618Gao, Z., Geilfus, N.-X., Saiz-Lopez, A., & Wang, F. (2022). Reproducing Arctic springtime tropospheric ozone and mercury depletion events in an outdoor mesocosm sea ice facility. *Atmospheric Chemistry and Physics*, *22*(3), 1811–1824. https://doi.org/10.5194/acp-22-1811-2022Gelaro, R., McCarty, W., Suárez, M. J., Todling, R., Molod, A., Takacs, L., et al. (2017). The Modern-Era Retrospective Analysis for Research and Applications, Version 2 (MERRA-2). *Journal of Climate*, *30*(14), 5419–5454. https://doi.org/10.1175/JCLI-D-16-0758.1Global Modeling And Assimilation Office, & Pawson, Steven. (2015). MERRA-2 inst3_3d_asm_Nv: 3d,3-Hourly,Instantaneous,Model-Level,Assimilation,Assimilated Meteorological Fields V5.12.4 [Data set]. NASA Goddard Earth Sciences Data and Information Services Center. https://doi.org/10.5067/WWQSXQ8IVFW8Halfacre, J. W., Knepp, T. N., Shepson, P. B., Thompson, C. R., Pratt, K. A., Li, B., et al. (2014). Temporal and spatial characteristics of ozone depletion events from measurements in the Arctic. *Atmospheric Chemistry and Physics*, *14*(10), 4875–4894. https://doi.org/10.5194/acp-14-4875-2014Hendrick, F., Van Roozendael, M., Chipperfield, M. P., Dorf, M., Goutail, F., Yang, X., et al. (2007). Retrieval of stratospheric and tropospheric BrO profiles and columns using ground-based zenith-sky DOAS observations at Harestua, 60°N. *Atmospheric Chemistry and Physics Discussions*, *7*(3), 8663–8708. https://doi.org/10.5194/acpd-7-8663-2007Hendrick, F., Rozanov, A., Johnston, P. V., Bovensmann, H., De Mazière, M., Fayt, C., et al. (2009). Multi-year comparison of stratospheric BrO vertical profiles retrieved from SCIAMACHY limb and ground-based UV-visible measurements. *Atmospheric Measurement Techniques*, *2*(1), 273–285. https://doi.org/10.5194/amt-2-273-2009Herrmann, M., Sihler, H., Frieß, U., Wagner, T., Platt, U., & Gutheil, E. (2021). Time-dependent 3D simulations of tropospheric ozone depletion events in the Arctic spring using the Weather Research and Forecasting model coupled with Chemistry (WRF-Chem). *Atmospheric Chemistry and Physics*, *21*(10),

7611–7638. https://doi.org/10.5194/acp-21-7611-2021Hollwedel, J., Wenig, M., Beirle, S., Kraus, S., Kuhl, S., Wilms-Grabe, W., et al. (2004). Year-to-year variations of spring time polar tropospheric BrO as seen by GOME. *Advances in Space Research*, *34*, 804–808. https://doi.org/10.1016/j.asr.2003.08.060Holmes, C. D., Jacob, D. J., & Yang, X. (2006). Global lifetime of elemental mercury against oxidation by atomic bromine in the free troposphere. *Geophysical Research Letters*, *33*(20). https://doi.org/10.1029/2006GL027176Hu, L., Keller, C. A., Long, M. S., Sherwen, T., Auer, B., Da Silva, A., et al. (2018). Global simulation of tropospheric chemistry at 12.5 km resolution: performance and evaluation of the GEOS-Chem chemical module (v10-1) within the NASA GEOS Earth system model (GEOS-5 ESM). *Geoscientific Model Development*, *11*(11), 4603–4620. https://doi.org/10.5194/gmd-11-4603-2018Huang, J., Jaeglé, L., & Shah, V. (2018). Using CALIOP to constrain blowing snow emissions of sea salt aerosols over Arctic and Antarctic sea ice. *Atmospheric Chemistry and Physics*. https://doi.org/10.5194/acp-18-16253-2018Huang, J., Jaeglé, L., Chen, Q., Alexander, B., Sherwen, T., Evans, M. J., et al. (2020). Evaluating the impact of blowing-snow sea salt aerosol on springtime BrO and O_3 in the Arctic. *Atmospheric Chemistry and Physics*, *20*(12), 7335–7358. https://doi.org/10.5194/acp-20-7335-2020Jones, A. E., Anderson, P. S., Wolff, E. W., Turner, J., Rankin, A. M., & Colwell, S. R. (2006). A role for newly forming sea ice in springtime polar tropospheric ozone loss? Observational evidence from Halley station, Antarctica. *Journal of Geophysical Research*, *111*(D8), D08306. https://doi.org/10.1029/2005JD006566Jones, A. E., Anderson, P. S., Begoin, M., Brough, N., Hutterli, M. A., Marshall, G. J., et al. (2009). BrO, blizzards, and drivers of polar tropospheric ozone depletion events. *Atmospheric Chemistry and Physics*, *9*(14), 4639–4652. https://doi.org/10.5194/acp-9-4639-2009Keil, A. D., & Shepson, P. B. (2006). Chlorine and bromine atom ratios in the springtime Arctic troposphere as determined from measurements of halogenated volatile organic compounds. *Journal of Geophysical Research*, *111*(D17), D17303. https://doi.org/10.1029/2006JD007119Keller, C. A., Long, M. S., Yantosca, R. M., Da Silva, A. M., Pawson, S., & Jacob, D. J. (2014). HEMCO v1.0: a versatile, ESMF-compliant component for calculating emissions in atmospheric models. *Geoscientific Model Development*, *7*(4), 1409–1417. https://doi.org/10.5194/gmd-7-1409-2014Keller, Christoph A., Knowland, K. E., Duncan, B. N., Liu, J., Anderson, D. C., Das, S., et al. (2021). Description of the NASA GEOS Composition Forecast Modeling System GEOS-CF v1.0. *Journal of Advances in Modeling Earth Systems*, *13*(4). https://doi.org/10.1029/2020MS002413Knepp, T. N., Bottenheim, J., Carlsen, M., Carlson, D., Donohoue, D., Friederich, G., et al. (2010). Development of an autonomous sea ice tethered buoy for the study of ocean-atmosphere-sea ice-snow pack interactions: the O-buoy. *Atmospheric Measurement Techniques*, *3*(1), 249–261. https://doi.org/10.5194/amt-3-249-2010Knowland, K. E., Keller, C. A., Wales, P. A., Wargan, K., Coy, L., Johnson, M. S., et al. (2022). NASA GEOS Composition Forecast Modeling System GEOS-CF v1.0: Stratospheric composition. *Journal of Advances in Modeling Earth Systems*. https://doi.org/10.1029/2021MS002852Krotkov, N. A., Lamsal, L. N., Celarier,

E. A., Swartz, W. H., Marchenko, S. V., Bucsela, E. J., et al. (2017). The version 3 OMI NO_2 standard product. *Atmospheric Measurement Techniques*, *10*(9), 3133–3149. https://doi.org/10.5194/amt-10-3133-2017Levelt, P. F., Van den Oord, G. H. J., Dobber, M. R., Malkki, A., Visser, H., de Vries, J., et al. (2006). The Ozone Monitoring Instrument. *IEEE Transactions On Geoscience And Remote Sensing*, *44*(5), 1093–1101. https://doi.org/Urn:nbn:nl:ui:25-648485Liao, J., Huey, L. G., Liu, Z., Tanner, D. J., Cantrell, C. A., Orlando, J. J., et al. (2014). High levels of molecular chlorine in the Arctic atmosphere. *Nature Geoscience*, *7*(2), 91–94. https://doi.org/10.1038/ngeo2046Long, M. S., Yantosca, R., Nielsen, J. E., Keller, C. A., da Silva, A., Sulprizio, M. P., et al. (2015). Development of a grid-independent GEOS-Chem chemical transport model (v9-02) as an atmospheric chemistry module for Earth system models. *Geoscientific Model Development*, *8*(3), 595–602. https://doi.org/10.5194/gmd-8-595-2015Mahajan, A. S., Shaw, M., Oetjen, H., Hornsby, K. E., Carpenter, L. J., Kaleschke, L., et al. (2010). Evidence of reactive iodine chemistry in the Arctic boundary layer. *Journal of Geophysical Research*, *115*(D20), D20303. https://doi.org/10.1029/2009JD013665Marelle, L., Thomas, J. L., Ahmed, S., Tuite, K., Stutz, J., Dommergue, A., et al. (2021). Implementation and Impacts of Surface and Blowing Snow Sources of Arctic Bromine Activation Within WRF-Chem 4.1.1. *Journal of Advances in Modeling Earth Systems*, *13*(8). https://doi.org/10.1029/2020MS002391McClure-Begley, A., Petropavlovskikh, I., & Oltmans, S. J. (2014). Earth System Research Laboratory Ozone Water Vapor Group Surface Ozone Measurements [Data set]. NOAA National Centers for Environmental Information. https://doi.org/10.7289/V57P8WBFMcPeters, R., Kroon, M., Labow, G., Brinksma, E., Balis, D., Petropavlovskikh, I., et al. (2008). Validation of the Aura Ozone Monitoring Instrument total column ozone product. *Journal of Geophysical Research*, *113*(D15), D15S14. https://doi.org/10.1029/2007JD008802Oltmans, S. J., & Levy, H. (1994). Surface ozone measurements from a global network. *Atmospheric Environment*, *28*(1), 9–24. https://doi.org/10.1016/1352-2310(94)90019-1Oltmans, S. J., Schnell, R. C., Sheridan, P. J., Perterson, R. E., Li, S.-M., Winchester, J. W., et al. (1989). Seasonal surface ozone and filterable bromine realtionship in the high Artic. *Atmospheric Environment*, *23*(11), 2431–2441. https://doi.org/10.1016/0004-6981(89)90254-0Orbe, C., Oman, L. D., Strahan, S. E., Waugh, D. W., Pawson, S., Takacs, L. L., & Molod, A. M. (2017). Large-Scale Atmospheric Transport in GEOS Replay Simulations. *Journal of Advances in Modeling Earth Systems*, *9*(7), 2545–2560. https://doi.org/10.1002/2017MS001053Peterson, P. K., Simpson, W. R., Pratt, K. A., Shepson, P. B., Frie\s s, U., Zielcke, J., et al. (2015). Dependence of the vertical distribution of bromine monoxide in the lower troposphere on meteorological factors such as wind speed and stability. *Atmospheric Chemistry and Physics*, *15*(4), 2119–2137. https://doi.org/10.5194/acp-15-2119-2015Platt, S. M., Hov, Ø., Berg, T., Breivik, K., Eckhardt, S., Eleftheriadis, K., et al. (2021). Atmospheric composition in the European Arctic and 30 years of the Zeppelin Observatory, Ny-Ålesund. https://doi.org/10.5194/acp-2021-505Platt, U., & Stutz, J. (2008). *Differential Optical Absorption*

Spectroscopy.Pratt, K. A. (2019). Tropospheric Halogen Photochemistry in the Rapidly Changing Arctic. *Trends in Chemistry*, *1*(6), 545–548. https://doi.org/10.1016/j.trechm.2019.06.001Pratt, K. A., Custard, K. D., Shepson, P. B., Douglas, T. A., Pöhler, D., General, S., et al. (2013). Photochemical production of molecular bromine in Arctic surface snowpacks. *Nature Geoscience*, *6*(5), 351–356. https://doi.org/10.1038/ngeo1779Raso, A. R. W., Custard, K. D., May, N. W., Tanner, D., Newburn, M. K., Walker, L., et al. (2017). Active molecular iodine photochemistry in the Arctic. *Proceedings of the National Academy of Sciences*, *114*(38), 10053–10058. https://doi.org/10.1073/pnas.1702803114Richter, A., Wittrock, F., Eisinger, M., & Burrows, J. P. (1998). GOME observations of tropospheric BrO in northern hemispheric spring and summer 1997. *Geophysical Research Letters*, *25*(14), 2683–2686. https://doi.org/10.1029/98GL52016Rodgers, C. D. (2000). *Inverse methods for atmospheric sounding: theory and practice*. Singapore: World Scientific.Saiz-Lopez, A., & von Glasow, R. (2012). Reactive halogen chemistry in the troposphere. *Chemical Society Reviews*, *41*(19), 6448. https://doi.org/10.1039/c2cs35208gSaiz-Lopez, A., Plane, J. M. C., Baker, A. R., Carpenter, L. J., von Glasow, R., Gómez Martín, J. C., et al. (2012). Atmospheric Chemistry of Iodine. *Chemical Reviews*, *112*(3), 1773–1804. https://doi.org/10.1021/cr200029uSalawitch, R. J., Canty, T., Kurosu, T., Chance, K., Liang, Q., Da Silva, A., et al. (2010). A new interpretation of total column BrO during Arctic spring. *Geophysical Research Letters*, *37*(21), 1–9. https://doi.org/10.1029/2010GL043798Schenkeveld, V. M. E., Jaross, G., Marchenko, S., Haffner, D., Kleipool, Q. L., Rozemeijer, N. C., et al. (2017). In-flight performance of the Ozone Monitoring Instrument. *Atmospheric Measurement Techniques*, *10*(5), 1957–1986. https://doi.org/10.5194/amt-10-1957-2017Schmidt, J. A., Jacob, D. J., Horowitz, H. M., Hu, L., Sherwen, T., Evans, M. J., et al. (2016). Modeling the observed tropospheric BrO background: Importance of multiphase chemistry and implications for ozone, OH, and mercury. *Journal of Geophysical Research: Atmospheres*, *121*(19), 11,819-11,835. https://doi.org/10.1002/2015JD024229Schofield, R., Kreher, K., Conner, B. J., Johnston, P. V., Thomas, A., Shooter, D., et al. (2004). Retrieved tropospheric and stratospheric BrO columns over Lauder, New Zealand. *Journal of Geophysical Research*, *109*(D14), D14304. https://doi.org/10.1029/2003JD004463Schroeder, W. H., Anlauf, K. G., Barrie, L. A., Lu, J. Y., Steffen, A., Schneeberger, D. R., & Berg, T. (1998). Arctic springtime depletion of mercury. *Nature*, *394*(6691), 331–332. https://doi.org/10.1038/28530Seo, S., Richter, A., Blechschmidt, A.-M., Bougoudis, I., & Burrows, J. P. (2019). First high-resolution BrO column retrievals from TROPOMI. *Atmospheric Measurement Techniques*, *12*(5), 2913–2932. https://doi.org/10.5194/amt-12-2913-2019Seo, S., Richter, A., Blechschmidt, A.-M., Bougoudis, I., & Burrows, J. P. (2020). Spatial distribution of enhanced BrO and its relation to meteorological parameters in Arctic and Antarctic sea ice regions. *Atmospheric Chemistry and Physics*, *20*(20), 12285–12312. https://doi.org/10.5194/acp-20-12285-2020Sherwen, T., Schmidt, J. A., Evans, M. J., Carpenter, L. J., Gro\s smann, K., Eastham, S. D., et

al. (2016). Global impacts of tropospheric halogens (Cl, Br, I) on oxidants and composition in GEOS-Chem. *Atmospheric Chemistry and Physics*, *16*(18), 12239–12271. https://doi.org/10.5194/acp-16-12239-2016Sihler, H., Platt, U., Beirle, S., Marbach, T., Kühl, S., Dörner, S., et al. (2012). Tropospheric BrO column densities in the Arctic derived from satellite: Retrieval and comparison to ground-based measurements. *Atmospheric Measurement Techniques*, *5*(11), 2779–2807. https://doi.org/10.5194/amt-5-2779-2012Simpson, W. R., von Glasow, R., Riedel, K., Anderson, P., Ariya, P., Bottenheim, J., et al. (2007). Halogens and their role in polar boundary-layer ozone depletion. *Atmospheric Chemistry and Physics*, *7*(16), 4375–4418. https://doi.org/10.5194/acp-7-4375-2007Simpson, W. R., Perovich, D., Matrai, P., Shepson, P., & Chavez, F. (2009). The Collaborative O-Buoy Project: Deployment of a Network of Arctic Ocean Chemical Sensors for the IPY and beyond [Text/xml]. Arctic Data Center. https://doi.org/10.18739/A2WD4WSimpson, W. R., Brown, S. S., Saiz-Lopez, A., Thornton, J. A., & Von Glasow, R. (2015). Tropospheric Halogen Chemistry: Sources, Cycling, and Impacts. *Chemical Reviews*, *115*(10), 4035–4062. https://doi.org/10.1021/cr5006638Simpson, W. R., Peterson, P. K., Frie\s s, U., Sihler, H., Lampel, J., Platt, U., et al. (2017). Horizontal and vertical structure of reactive bromine events probed by bromine monoxide MAX-DOAS. *Atmospheric Chemistry and Physics*, *17*(15), 9291–9309. https://doi.org/10.5194/acp-17-9291-2017Sioris, C. E., Kovalenko, L. J., McLinden, C. A., Salawitch, R. J., Van Roozendael, M., Goutail, F., et al. (2006). Latitudinal and vertical distribution of bromine monoxide in the lower stratosphere from Scanning Imaging Absorption Spectrometer for Atmospheric Chartography limb scattering measurements. *Journal of Geophysical Research*, *111*(D14), D14301. https://doi.org/10.1029/2005JD006479Spurr, R. J. D., Kurosu, T. P., & Chance, K. V. (2001). A linearized discrete ordinate radiative transfer model for atmospheric remote-sensing retrieval. *Journal of Quantitative Spectroscopy and Radiative Transfer*, *68*(6), 689–735. https://doi.org/10.1016/S0022-4073(00)00055-8Stephens, C. R., Shepson, P. B., Steffen, A., Bottenheim, J. W., Liao, J., Huey, L. G., et al. (2012). The relative importance of chlorine and bromine radicals in the oxidation of atmospheric mercury at Barrow, Alaska: MERCURY OXIDATION IN THE ARCTIC. *Journal of Geophysical Research: Atmospheres*, *117*(D14), n/a-n/a. https://doi.org/10.1029/2011JD016649Strahan, S. E., Duncan, B. N., & Hoor, P. (2007). Observationally derived transport diagnostics for the lowermost stratosphere and their application to the GMI chemistry and transport model. *Atmospheric Chemistry and Physics*, *7*, 2435–2445. https://doi.org/10.5194/acpd-7-1449-2007Suleiman, R. M., Chance, K., Liu, X., González Abad, G., Kurosu, T. P., Hendrick, F., & Theys, N. (2019). OMI total bromine monoxide (OMBRO) data product: algorithm, retrieval and measurement comparisons. *Atmospheric Measurement Techniques*, *12*(4), 2067–2084. https://doi.org/10.5194/amt-12-2067-2019Swanson, W. F., Graham, K. A., Halfacre, J. W., Holmes, C. D., Shepson, P. B., & Simpson, W. R. (2020). Arctic Reactive Bromine Events Occur in Two Distinct Sets of Environmental Conditions: A Statistical Analysis of 6

Years of Observations. *Journal of Geophysical Research: Atmospheres*, *125*(10). https://doi.org/10.1029/2019JD032139Swanson, W. F., Holmes, C. D., Simpson, W. R., Confer, K., Marelle, L., Thomas, J. L., et al. (2022). *Comparison of model and ground observations finds snowpack and blowing snow both contribute to Arctic tropospheric reactive bromine* (preprint). Gases/Atmospheric Modelling/Troposphere/Chemistry (chemical composition and reactions). https://doi.org/10.5194/acp-2022-44Theys, N., Van Roozendael, M., Errera, Q., Hendrick, F., Daerden, F., Chabrillat, S., et al. (2009). A global stratospheric bromine monoxide climatology based on the BASCOE chemical transport model. *Atmospheric Chemistry and Physics*, *9*(3), 831–848. https://doi.org/10.5194/acp-9-831-2009Theys, N., Van Roozendael, M., Hendrick, F., Yang, X., De Smedt, I., Richter, A., et al. (2011). Global observations of tropospheric BrO columns using GOME-2 satellite data. *Atmospheric Chemistry and Physics*, *11*(4), 1791–1811. https://doi.org/10.5194/acp-11-1791-2011Thompson, C. R., Shepson, P. B., Liao, J., Huey, L. G., Apel, E. C., Cantrell, C. A., et al. (2015). Interactions of bromine, chlorine, and iodine photochemistry during ozone depletions in Barrow, Alaska. *Atmospheric Chemistry and Physics*, *15*(16), 9651–9679. https://doi.org/10.5194/acp-15-9651-2015Toyota, K., McConnell, J. C., Lupu, A., Neary, L., McLinden, C. A., Richter, A., et al. (2011). Analysis of reactive bromine production and ozone depletion in the Arctic boundary layer using 3-D simulations with GEM-AQ: inference from synoptic-scale patterns. *Atmospheric Chemistry and Physics*, *11*(8), 3949–3979. https://doi.org/10.5194/acp-11-3949-2011Van Roozendael, M., Wagner, T., Richter, A., Pundt, I., Arlander, D. W., Burrows, J. P., et al. (2002). Intercomparison of BrO measurements from ERS-2 GOME, ground-based and balloon platforms. *Advances in Space Research*, *29*(11), 1661–1666. https://doi.org/10.1016/S0273-1177(02)00098-4Vasilkov, A., Joiner, J., Spurr, R., Bhartia, P. K., Levelt, P., & Stephens, G. (2008). Evaluation of the OMI cloud pressures derived from rotational Raman scattering by comparisons with other satellite data and radiative transfer simulations. *Journal of Geophysical Research*, *113*(D15), D15S19. https://doi.org/10.1029/2007JD008689Vasilkov, A., Joiner, J., Haffner, D., Bhartia, P. K., & Spurr, R. J. D. (2010). What do satellite backscatter ultraviolet and visible spectrometers see over snow and ice? A study of clouds and ozone using the A-train. *Atmospheric Measurement Techniques*, *3*(3), 619–629. https://doi.org/10.5194/amt-3-619-2010Wagner, T., & Platt, U. (1998). Satellite mapping of enhanced BrO concentrations in the troposphere. *Nature*, *395*(6701), 486–490. https://doi.org/10.1038/26723Wales, P. A., Salawitch, R. J., Lind, E. S., Mount, G. H., Canty, T. P., Chance, K., et al. (2021). Evaluation of the Stratospheric and Tropospheric Bromine Burden Over Fairbanks, Alaska Based on Column Retrievals of Bromine Monoxide. *Journal of Geophysical Research Atmospheres*, *126*(2), e2020JD032896. https://doi.org/10.1029/2020JD032896Wang, X., Jacob, D. J., Downs, W., Zhai, S., Zhu, L., Shah, V., et al. (2021). Global tropospheric halogen (Cl, Br, I) chemistry and its impact on oxidants. *Atmospheric Chemistry and Physics*, *21*(18), 13973–13996. https://doi.org/10.5194/acp-21-13973-2021Wennberg, P. (1999). Bromine explosion. *Nature*, *397*(6717),

299–301. https://doi.org/10.1038/16805Wessel, S., Aoki, S., Winkler, P., Weller, R., Herber, A., Gernandt, H., & Schrems, O. (1998). Tropospheric ozone depletion in polar regions A comparison of observations in the Arctic and Antarctic. *Tellus B: Chemical and Physical Meteorology*, *50*(1), 34–50. https://doi.org/10.3402/tellusb.v50i1.16020Wilmouth, D. M., Hanisco, T. F., Donahue, N. M., & Anderson, J. G. (1999). Fourier Transform Ultraviolet Spectroscopy of the A 2Π3/2 ← X 2Π3/2 Transition of BrO. *The Journal of Physical Chemistry A*, *103*(45), 8935–8945. https://doi.org/10.1021/jp991651oYang, X., Cox, R. A., Warwick, N. J., Pyle, J. A., Carver, G. D., O'Connor, F. M., & Savage, N. H. (2005). Tropospheric bromine chemistry and its impacts on ozone: A model study. *Journal of Geophysical Research Atmospheres*, *110*(23), 1–18. https://doi.org/10.1029/2005JD006244Yang, X., Pyle, J. A., Cox, R. A., Theys, N., & Van Roozendael, M. (2010). Snow-sourced bromine and its implications for polar tropospheric ozone. *Atmospheric Chemistry and Physics*, *10*(16), 7763–7773. https://doi.org/10.5194/acp-10-7763-2010Yang, X., Blechschmidt, A.-M., Bognar, K., McClure-Begley, A., Morris, S., Petropavlovskikh, I., et al. (2020). Pan-Arctic surface ozone: modelling vs. measurements. *Atmospheric Chemistry and Physics*, *20*(24), 15937–15967. https://doi.org/10.5194/acp-20-15937-2020Zhao, T. L., Gong, S. L., Bottenheim, J. W., McConnell, J. C., Sander, R., Kaleschke, L., et al. (2008). A three-dimensional model study on the production of BrO and Arctic boundary layer ozone depletion. *Journal of Geophysical Research*, *113*(D24), D24304. https://doi.org/10.1029/2008JD010631Zhao, X., Strong, K., Adams, C., Schofield, R., Yang, X., Richter, A., et al. (2016). A case study of a transported bromine explosion event in the Canadian high arctic. *Journal of Geophysical Research: Atmospheres*, *121*(1), 457–477. https://doi.org/10.1002/2015JD023711Zhu, L., Jacob, D. J., Eastham, S. D., Sulprizio, M. P., Wang, X., Sherwen, T., et al. (2019). Effect of sea salt aerosol on tropospheric bromine chemistry. *Atmospheric Chemistry and Physics*, *19*(9), 6497–6507. https://doi.org/10.5194/acp-19-6497-2019